

Mercury's Polar Deposits

NANCY L. CHABOT, DAVID J. LAWRENCE, GREGORY A. NEUMANN, WILLIAM C. FELDMAN, AND DAVID A. PAIGE

13.1 INTRODUCTION

Two and a half decades ago, the discovery of Mercury's polar deposits provided the first evidence for the possibility of water ice on the solar system's innermost planet. Radar observations in 1991 with the Goldstone 70-m radio antenna as the transmitter and the Very Large Array as the receiving instrument revealed a highly reflective region near Mercury's north pole with a high same-sense to opposite-sense circular polarization ratio (Slade et al., 1992). The high reflectivity and circular polarization ratio of the observed radar-bright feature resembled the distinctive radar characteristics of the icy Galilean satellites (Campbell et al., 1978; Ostro et al., 1980; Hapke, 1990; Hapke and Blewett, 1991) and at the south polar cap of Mars (Muhleman et al., 1991), and so were interpreted as evidence for ice in Mercury's north polar region. The north polar radar-bright feature was subsequently identified in Arecibo observations, confirming the Goldstone discovery, and soon afterwards Arecibo observations led to the discovery of a south polar radar-bright feature as well (Harmon and Slade, 1992). In particular, the south polar radar-bright feature was estimated to lie within the large impact crater Chao Meng-Fu, suggesting that the radar-bright material favored the shadowed, low-temperature environment of this crater's interior, a setting consistent with the presence of long-lived water ice on Mercury. Evidence for the presence of water ice was also supported by thermal model calculations, which showed that the maximum temperatures in permanently shadowed regions within high-latitude craters on Mercury could provide thermal environments where water ice is stable for billions of years (Paige et al., 1992; Ingersoll et al., 1992). Analysis of the radar data further indicated that the water ice deposits are at least several meters in depth and that the ice layer itself must be very pure, with less than about 5% silicates by volume, leading to the suggestion that the ice was deposited on Mercury over a relatively short period of time (Butler et al., 1993).

Water ice within permanently shadowed cold traps had previously been proposed on theoretical grounds for the Moon (Urey, 1952; Watson et al., 1961) and also for Mercury (Thomas, 1974), but the Earth-based radar measurements of Mercury provided the first observational evidence to support the presence of such deposits. In contrast, Earth-based radar observations of the Moon did not reveal similar polar deposits (Stacy et al., 1997). Subsequent Earth-based radar measurements greatly improved the spatial resolution of the Mercury radar images, resolving many individual radar-bright spots near both of Mercury's poles and confirming the high radar

reflectivity and circular polarization ratio of the features (Harmon et al., 1994, 2001, 2011; Harcke, 2005; Harmon, 2007). Many radar-bright deposits were identified as lying within specific impact craters imaged by Mariner 10 in 1974–1975, but many other radar-bright features could not be mapped to craters or other geologic features because Mariner 10 acquired images covering only slightly less than half of Mercury's polar regions (Davies et al., 1978).

In parallel with the acquisition of radar images of Mercury's polar regions at increasingly improved resolution, more detailed modeling refined the quantitative understanding of the thermal environments of candidate host craters. Large permanently shadowed craters near the poles, such as Chao Meng-Fu, were concluded to have maximum surface temperatures conducive to the long-term stability of water ice at the surface (Salvail and Fanale, 1994; Vasavada et al., 1999). In contrast, the many radar-bright host craters located more than about 10° in latitude from the pole were found to have maximum surface temperatures that exceeded 110 K, and under such conditions water ice at the surface would be rapidly lost to thermal sublimation (Vasavada et al., 1999). However, burial of the deposits below a layer tens of centimeters thick was found to insulate water ice deposits to the point that they could remain stable for billions of years (Vasavada et al., 1999). Radar observations acquired at different wavelengths also were suggestive of a thin layer covering the deposits (Harmon et al., 2011). Although a thin layer of overlying regolith could enable water ice deposits to be thermally stable, how the deposits were buried sufficiently rapidly to prevent the complete loss of water ice at expected rates of impact gardening of the regolith was seen to be problematic (Harmon et al., 2001). An alternate suggestion was that a slightly dirty ice deposit might sublimate until its contaminant load formed a thin insulating lag deposit at the surface (Vasavada et al., 1999).

Small, simple craters on Mercury, which have diameters generally <10 km, posed a separate thermal challenge. Thermal models suggested that such craters could not host thermally stable water ice if located more than 2° in latitude from the poles, even if such deposits were buried by an insulating layer (Vasavada et al., 1999), yet Earth-based radar observations identified small craters farther from the pole that host radar-bright deposits (Harmon et al., 2001). Additionally, radar-bright features were discovered at latitudes as far from the pole as 67°N (Harmon et al., 2001), locations at which interior conditions were thought to present potentially challenging thermal environments for the stability of water ice, though the geologic setting of the majority of these lower-latitude deposits

could not be identified as they were in the hemisphere of the planet not imaged by Mariner 10.

Overall, Arecibo observations showed that Mercury's radar-bright deposits are extensive, covering $\sim 12,500 \text{ km}^2$ in the north polar region, with comparable deposits also in the south (Harmon et al., 2011), motivating questions about the formation and evolution of the material if it consists mostly of water ice. Simulations showed that water ice could migrate to cold traps at Mercury's poles with $\sim 10\%$ efficiency (Butler, 1997) and suggested that asteroids, comets, or interplanetary dust could have provided sufficient water to account for Mercury's radar-bright deposits, though impacts by a few large comets or asteroids were favored (Moses et al., 1999). From models of burial by regolith gardening, it was concluded that Mercury's polar deposits must have been emplaced geologically recently, within the last 50 Myr, in order that such deposits not be more deeply buried (Crider and Killen, 2005). Materials other than water ice were also suggested for the radar-bright deposits, including sulfur (Sprague et al., 1995) and silicates with dielectric properties altered at very low temperatures (Starukhina, 2001). The stark contrast between Mercury's extensive radar-bright deposits and the lack of any similar deposits on the Moon also raised a question. Thus, Earth-based radar observations and Mariner 10 images provided provocative but limited evidence to constrain the nature of Mercury's radar-bright polar deposits.

One of the six major science questions that motivated the MESSENGER mission (Chapter 1) was "What are the radar-reflective materials at Mercury's poles?" In the course of the mission's more than four Earth years of operations in orbit about Mercury, MESSENGER acquired multiple data sets to address this question. In this chapter, we review MESSENGER's observations of Mercury's polar deposits and discuss the resulting implications.

13.2 MESSENGER OBSERVATIONS OF MERCURY'S POLAR DEPOSITS

13.2.1 Mapping Results and Illumination Conditions

Whereas MESSENGER's three flybys of Mercury were equatorial and did not provide new views of Mercury's polar regions, upon entering orbit about Mercury, MESSENGER provided complete imaging of Mercury's surface with its Mercury Dual Imaging System (MDIS) (Hawkins et al., 2007). This global imaging enabled the first complete identification of the geologic features that host radar-bright deposits.

One of the earliest studies completed in orbit regarding Mercury's polar regions was a mapping of regions of permanent shadow near Mercury's south pole (Chabot et al., 2012). The MESSENGER spacecraft had a highly eccentric orbit about Mercury, which during the mission's first year of orbital operations had a minimum altitude of $\sim 200 \text{ km}$ in Mercury's northern hemisphere and a maximum altitude of $15,000 \text{ km}$ in the southern hemisphere (Chapter 1). At the higher altitudes, MDIS's wide-angle camera (WAC) was able to capture the entire sunlit region from Mercury's south pole to a latitude of $\sim 73^\circ\text{S}$ in a single image. Such imaging was repeated approximately every

other Earth day, for an entire Mercury solar day (176 Earth days), producing a data set of 89 images that captured Mercury's south polar region at a spatial scale of 1.7 km/pixel under all illumination conditions. By thresholding each image into sunlit and shadowed regions, an illumination map of Mercury's south polar region was created, as shown in Figure 13.1.

Many regions of permanent shadow from 73°S to the south pole are evident in Figure 13.1, covering a total area of $\sim 43,000 \text{ km}^2$. It is Mercury's low obliquity of 2.04 arcminutes (0.034°) (Margot et al., 2012) that accounts for the large area of terrain in shadow during a solar day. Moreover, regions in shadow in a single solar day remain in shadow indefinitely because the obliquity is stabilized by Mercury's 3:2 spin-orbit resonance, and these shadowed regions likely date to the times of formation of their host craters given that Mercury was probably captured into its current spin-orbit resonance early in solar system history (Peale, 1988).

The highest-resolution Earth-based radar image obtained of Mercury's south polar region is also shown in Figure 13.1. These data were acquired on 24–25 March 2005 at the Arecibo Observatory in S-band (12.6-cm wavelength) with a range resolution of 1.5 km (Harmon et al., 2011). All of the Arecibo radar-bright features either collocate with the regions identified as permanently shadowed or are within a few kilometers of an area of permanent shadow, consistent with the registration and resolution limitations of the MDIS and Arecibo data sets (Chabot et al., 2012). As originally identified by Harmon and Slade (1992), the $\sim 180\text{-km}$ -diameter crater Chao Meng-Fu hosts an extensive radar-bright deposit, which is both the largest radar-bright region and the largest permanently shadowed area on the entire planet.

Goldstone X-band (3.5-cm wavelength) radar observations have also been acquired of Mercury's south polar region, with a range resolution of 6 km (Harcke, 2005). Though the Goldstone data are lower in resolution than the Arecibo observations, they were acquired from a viewing direction nearly opposite to that of the 2005 Arecibo image and were used to catalog radar-bright features beyond the Arecibo radar horizon of the 2005 observations. All of the Goldstone radar-bright features also correspond to areas identified as in permanent shadow from the MDIS data set (Chabot et al., 2012).

Given MESSENGER's highly eccentric orbit, images acquired of Mercury's north polar region were at considerably higher resolution than those of the south polar region, allowing detailed identification of geologic features that host radar-bright deposits. However, a single MDIS WAC image could not capture the entire sunlit northern polar region to enable mapping of permanently shadowed regions, as was completed for Mercury's south polar region. Instead, from $\sim 6,500$ images of Mercury's north polar region that were acquired during MESSENGER's one-year primary orbital mission, regions of "persistent shadow" – meaning surfaces in shadow during all images acquired – were identified (Chabot et al., 2013). Even from this limited one-year data set, radar-bright features in Mercury's north polar region (Harmon et al., 2011) were found to be associated with locations persistently shadowed in MDIS images. Subsequently, with over $16,000$ images from MESSENGER's full orbital mission, Deutsch et al. (2016)

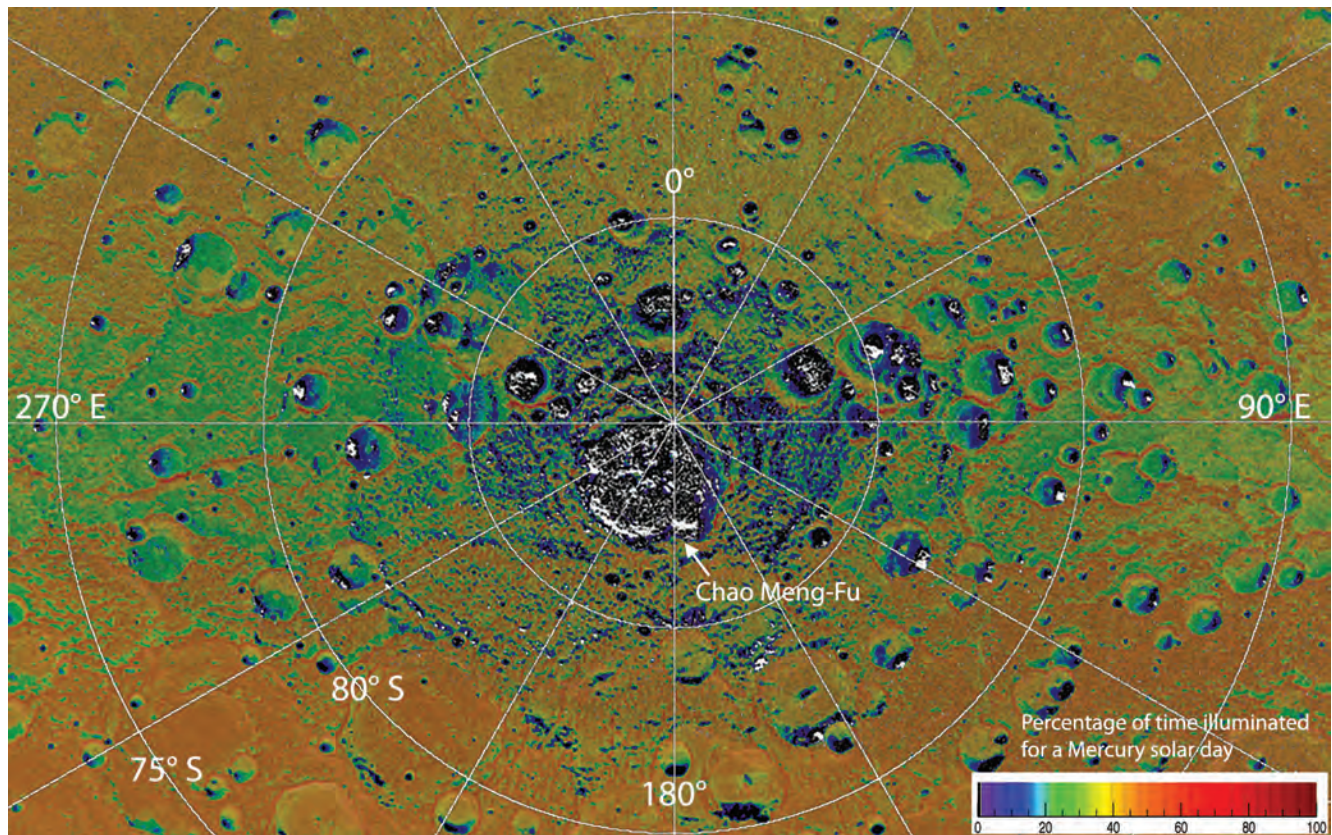


Figure 13.1. Mercury's south polar region colored by the percentage of illumination time (Chabot et al., 2012), with areas of high radar backscatter in the highest-resolution Arecibo radar image (Harmon et al., 2011) overlain in white.

further confirmed the association of radar-bright and persistently shadowed regions and substantially improved the identification of persistently shadowed regions within 4° of the north pole.

Additionally, the lower spacecraft altitude enabled topographic measurements by MESSENGER's Mercury Laser Altimeter (MLA) (Cavanaugh et al., 2007) at northern high latitudes that were not possible at comparable latitudes in the south. The solar illumination at Mercury's north polar region was modeled with MLA topographic data in a manner similar to that used to investigate permanently shadowed regions on the Moon (Mazarico et al., 2011), and regions of permanent shadow were identified from insolation models independent of the imaging data (Mazarico et al., 2014; Deutsch et al., 2016). Figure 13.2 shows the regions modeled as permanently shadowed with an MLA-based elevation model obtained from data acquired over MESSENGER's full orbital mission. There is good agreement between regions mapped as permanently shadowed by MLA and persistently shadowed by MDIS (Deutsch et al., 2016).

Also shown in Figure 13.2 is the highest-resolution radar image yet produced of Mercury's north polar region, with a range resolution of 1.5 km (Harmon et al., 2011). The radar image was assembled from multiple Arecibo observations obtained at S-band from 1999 to 2005, covering a wide range of viewing geometries that serve to reduce regions in radar shadow or beyond the radar horizon, in contrast to the south pole radar image of Figure 13.1 that was obtained from a single

observing run. As seen in Figure 13.2, all of the well-defined radar-bright features near Mercury's north pole are associated with regions of permanent shadow.

Although all of the radar-bright features near both of Mercury's poles are associated with permanently shadowed regions, not all permanently shadowed regions also host radar-bright features. For water ice deposits, permanent shadow is a necessary but not sufficient condition to host such material, as the temperature within permanently shadowed regions can still be too high for the long-term stability of water ice, depending on the host crater's shape, latitude, longitude, and other factors (Paige et al., 1992; Vasavada et al., 1999). However, for permanently shadowed regions within complex craters located within 10° of the pole, the thermal environment is expected to be generally conducive to the long-term stability of surface or buried water ice (Vasavada et al., 1999). On Mercury, the transition with increasing diameter between simple and complex crater morphologies for primary craters occurs at a diameter of ~ 10 km (Pike, 1988; Barnouin et al., 2012; Susorney et al., 2016). For craters >10 km in diameter within 10° of Mercury's north pole that also contain regions of permanent shadow, 65% host radar-bright deposits (Deutsch et al., 2016). Similarly, in the south polar region, most, but not all, shadowed craters host radar-bright deposits (Chabot et al., 2012). In the north polar region, for example, Burke (29-km diameter) and Sapkota (27-km diameter) craters, labeled in Figure 13.2, have interiors that are almost in complete shadow, yet neither hosts an extensive radar-bright deposit, in contrast to similarly sized

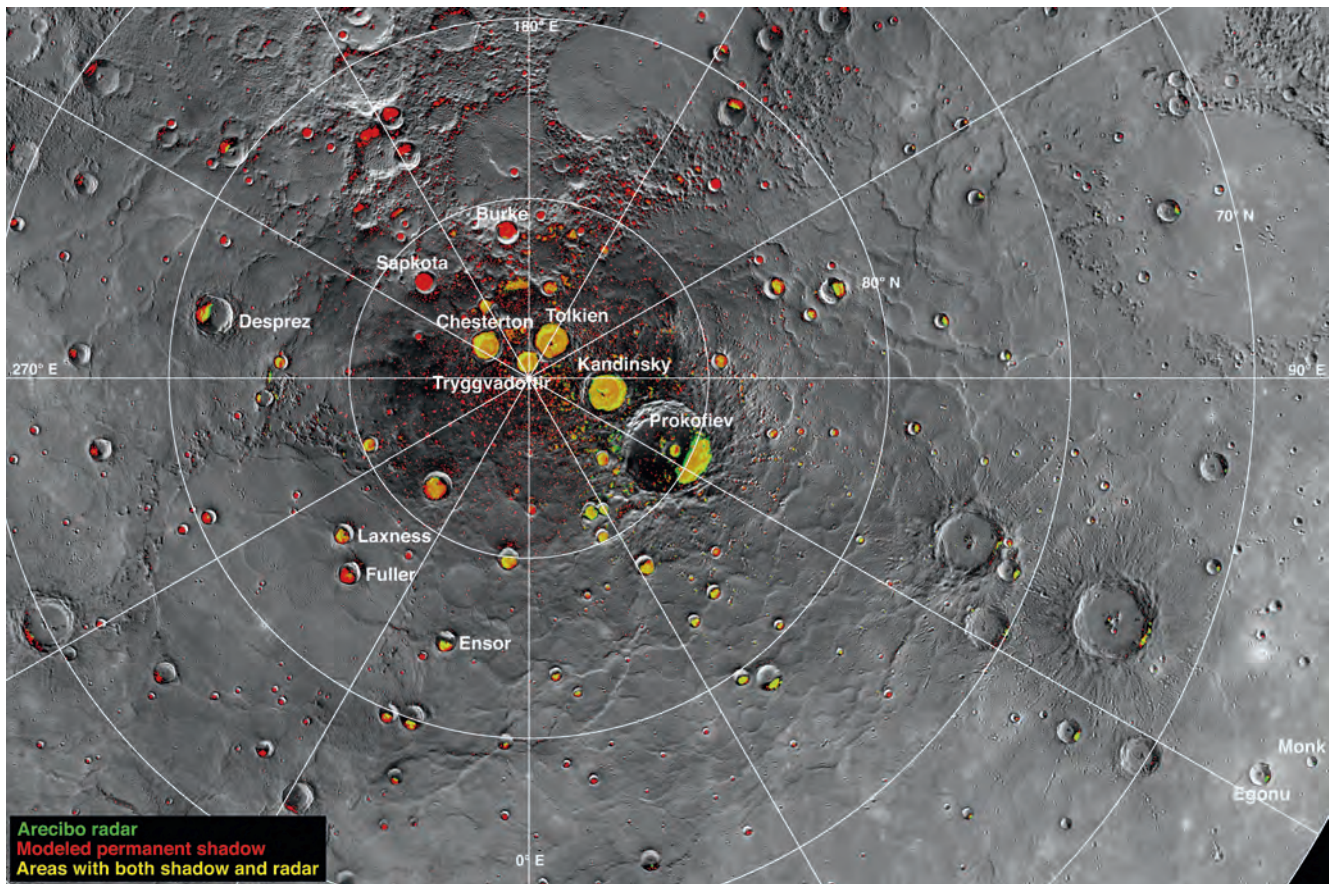


Figure 13.2. A MESSENGER mosaic of Mercury's north polar region, overlain with the highest-resolution Arecibo radar image in green (Harmon et al., 2011) and with a map of regions of permanent shadow in red (Deutsch et al., 2016). Regions that are both in permanent shadow and radar-bright are colored yellow.

neighboring craters. Thus, Burke, Sapkota, and other craters may lack radar-bright deposits, indicating that not all of Mercury's available cold-traps are currently occupied by water ice. Alternatively, such deposits may be present but were not observed during the Arecibo measurements or are buried too deep to be detected. As discussed by Deutsch et al. (2016), consideration of the Arecibo radar viewing opportunities does not support the view that the lack of extensive radar-bright deposits in these craters is a result of limited radar coverage, though the observed longitudinal distribution of permanently shadowed craters that lack radar-bright deposits is not correlated with thermal conditions, possibly suggesting some sort of viewing or detection limitation with the radar observations.

Because of Mercury's 3:2 spin-orbit resonance, the "hot pole" longitudes of 0°E and 180°E always experience local noon at Mercury's perihelion, resulting in a ~130 K higher temperature at the equator than experienced for local noon at the "cold pole" longitudes of 90°E and 270°E (Vasavada et al., 1999). For locations farther than 10° from the poles, there is a preference for radar-bright features to be located along the cold-pole longitudes, as noted from the radar observations (Harmon et al., 2001, 2011). MESSENGER observations have confirmed that for regions >10° latitude from the poles, the radar-bright deposits do not uniformly occupy all permanently shadowed regions but rather show a preference for longitudes near the 90°

E and 270°E cold-pole longitudes (Chabot et al., 2012, 2013). At these longitudes, radar-bright features have been identified in craters at latitudes a considerable distance from the poles; in the south, the most equatorward radar-bright deposit is at about 74° S (Figure 13.1), and in the north (Figure 13.2) Egonu (67°N) and Monk (66°N) are the lowest-latitude craters to host radar-bright deposits.

Thermal models prior to MESSENGER measurements indicated that the interiors of simple bowl-shaped craters experience considerably warmer temperatures than flatter-floored complex craters because of increased indirect heating from scattering off crater walls (Vasavada et al., 1999). From a model of an idealized bowl-shaped simple crater, <10 km in diameter with a depth-to-diameter ratio of 5:1, Vasavada et al. (1999) concluded that simple craters on Mercury cannot host long-lived water ice except if located within 2° latitude of the pole. MESSENGER images have shown that there are numerous radar-bright deposits within small craters <10 km in diameter located considerably farther from the poles than 2° in both the north and south polar regions (Chabot et al., 2012, 2013; Ernst et al., 2014; Deutsch et al., 2016), in addition to the few noted previously by Harmon et al. (2001) from Mariner 10 images. In particular, many of the small craters surrounding Prokofiev host radar-bright deposits, and secondary craters on Mercury are generally shallower than primary craters (Susorney et al., 2016). Assessments of the

morphology of these small craters from MLA measurements indicate that they are shallower than was assumed for the thermal model of Vasavada et al. (1999) (Ernst et al., 2014), which could affect the thermal stability of water ice in their shadowed interiors.

The thickness of the radar-bright deposits is poorly constrained. A minimum thickness of several meters is implied by the absence of a clear drop in radar cross section with increasing wavelength for observations at 3.5-cm, 12.6-cm and 70-cm wavelengths, indicating that the scattering layer is many wavelengths thick at all three wavelengths (Black et al., 2010). A maximum thickness of a few hundred meters has been estimated from statistical similarities between the depths and diameters of craters that host radar-bright deposits and those that do not, as determined by MLA measurements (Talpe et al., 2012). From a pre-MESSENGER study of 12 craters that host radar-bright deposits, Vilas et al. (2005) concluded that these craters were shallower than normal, but MESSENGER MLA measurements have not supported that result (Talpe et al., 2012), likely illustrating the greater accuracy of laser altimetry compared with topographic information derived from Mariner 10 imaging data. From a digital elevation model (DEM) produced from MLA measurements to compare the topography of six craters that host radar-bright deposits and six craters that do not, Eke et al. (2017) estimated a maximum thickness of the radar-bright deposits of 150 m, with a typical excess height associated with the radar-bright deposits of 50 ± 35 m (one standard deviation, or 1σ). From individual MLA tracks that cross the boundaries of two radar-bright deposits, Susorney et al. (2017) did not detect any statistically significant change in topography associated with the radar-bright deposits in either Prokofiev or Desprez craters, reporting deposit thickness limits of 33 ± 60 m and 45 ± 38 m, respectively (1σ uncertainties). Susorney et al. (2017) concluded that the natural topographic variability of the crater floors, e.g., from younger and smaller impact craters, boulders, and variations in impact melt thickness, may be on the same scale or larger than the thickness of the radar-bright deposits. Additionally, from a characterization of the depths and diameters of nine small impact craters imaged within radar-bright regions, Deutsch et al. (2017b) estimated that the radar-bright deposits in those regions may have a maximum thickness of 24–95 m if the small craters predate the emplacement of the radar-bright deposits. Overall, the fact that these studies have not been able to measure directly the thickness of the radar-bright deposits but rather have placed increasingly smaller limits on the maximum thickness suggest that the thickness of the radar-bright deposits may be toward the lower end of the current estimated range, e.g., tens of meters or even less.

13.2.2 Neutron Spectrometer Measurements

To test the hypothesis that Mercury's polar deposits are composed mostly of water, the MESSENGER spacecraft was equipped with a Neutron Spectrometer (NS) as part of the Gamma-Ray and Neutron Spectrometer instrument (Goldsten et al., 2007). Planetary neutron spectroscopy is a robust technique for measuring hydrogen concentrations on airless or nearly airless planetary bodies (Prettyman, 2007), and the high hydrogen abundance in water ice relative to other candidate radar

reflective materials allows neutron spectroscopy to constrain the radar-bright material (Feldman et al., 1997). This technique involves measurement of the neutrons created by nuclear spallation reactions when galactic cosmic rays (GCRs) strike a planetary surface. These neutrons have a broad spectrum of kinetic energy E_n that is typically divided into three energy ranges: thermal ($E_n < 0.4$ eV), epithermal (0.4 eV $< E_n < 0.5$ MeV), and fast ($E_n > 0.5$ MeV). A hydrogen atom has nearly the same mass as a neutron, which allows a highly efficient momentum transfer from the spallation neutrons, resulting in strong neutron moderation or downscatter in energy. This effect causes the number of epithermal neutrons to be depressed, so that variation of the epithermal count rate with location can be used as a sensitive indicator of the presence of hydrogen in planetary materials.

In contrast to techniques that measure surficial properties, such as spectral reflectance or X-ray spectroscopy, neutron spectroscopy is sensitive to the composition of planetary materials to a depth of tens of centimeters. Planetary epithermal neutrons were first measured at the Moon with the Lunar Prospector mission, and their fluxes permitted the conclusive identification of hydrogen enhancements at both lunar poles in the vicinity of permanently shadowed craters (Feldman et al., 1998). Neutron spectroscopy has also been used to measure and map hydrogen concentrations at Mars (Feldman et al., 2002) and the asteroid Vesta (Prettyman et al., 2012).

For Mercury, neutron spectroscopy provides a means to characterize the polar deposits that is complementary to other techniques in that it measures the bulk composition, in contrast to surface reflective (Section 13.2.3) or morphologic (Section 13.2.5) properties. If the radar-bright deposits are dominantly composed of hydrogen, then the polar regions should have an epithermal neutron flux that is lower than non-polar regions that have little to no hydrogen (Feldman et al., 1997). If, to the contrary, the radar-bright regions are dominantly composed of sulfur, as suggested by Sprague et al. (1995), then Mercury's polar regions should have a decreased thermal-neutron flux compared with non-polar regions but very little change in epithermal neutrons. Finally, if non-compositional effects, such as the alteration of the dielectric properties of silicate materials by unusually cold temperatures (Starukhina et al., 2001), are responsible for the radar-bright properties, then there should be no difference in neutron flux between polar and non-polar regions.

Although the neutron signatures for these different hypotheses are, in principle, clear and unambiguous, the actual neutron measurements proved to be challenging owing to several aspects of the MESSENGER mission. Planetary neutron measurements are generally count-rate limited, and therefore optimum measurements require specific measurement parameters. These parameters include close proximity to the target of interest (in this case the north polar radar-bright deposits), constant and/or regularly changing viewing geometry with a clear field of view to the target to enable simple and well-behaved viewing-geometry corrections, and multi-day to multi-week accumulation times to provide measurements with high statistical precision. Because MESSENGER operated at Mercury in an eccentric near-polar orbit with a constantly changing altitude and limited time near the north pole, and because of the multiple

types of measurements conducted by the MESSENGER spacecraft, the viewing geometry for the NS sensor was highly variable. None of the measurement parameters was fully optimized for NS observations. As a consequence, substantial analysis and data reduction were required to successfully obtain MESSENGER's north polar neutron measurements. From pre-orbit-insertion predictions of the orbital mission ephemeris, Lawrence et al. (2011) estimated that if the northern permanently shadowed regions contained extensive amounts of water ice, epithermal neutrons would show a count-rate decrease of 4% or less poleward of 60°–70°N compared with count rates at lower latitudes. The challenging aspect of this measurement was that this small signal variation had to be identified on top of systematic and non-compositional variations of between 200% and 300%. In addition, because of the spacecraft's high altitude (>200 km) above the radar-bright deposits, Lawrence et al. (2011) concluded that none of the radar-bright deposits would be individually spatially resolved, but rather the latitudinal variation of epithermal neutrons would be the primary signature of a polar hydrogen enhancement.

A full analysis of epithermal and fast neutron data from the first 10 months of the MESSENGER orbital mission was presented by Lawrence et al. (2013). The problem of detecting a <4% signal within the >200% non-compositional variations was solved by carrying out a quantitative simulation of the NS neutron-detection performance. This simulation accounted for the planetary neutron creation and transport with the Monte Carlo particle transport code MCNPX (Pelowitz et al., 2005). The neutron transport from the planet to the spacecraft was calculated from the analytic expressions of Feldman et al. (1989). Finally, the angular- and energy-dependent response of the NS was modeled with an MCNPX-based geometry model of the full MESSENGER spacecraft. Further details of these simulations were given by Lawrence et al. (2011, 2013).

The measured epithermal neutron count-rate data were compared with simulated rates for two end-member cases of hydrogen concentrations within the polar deposits identified by Earth-based radar: 100 wt% water-equivalent hydrogen (WEH) and 0 wt% WEH. This comparison is shown in Figure 13.3a, where the measured and simulated values are plotted versus latitude. The monotonic equator-to-pole variation is due mostly to the latitude-dependent radial neutron-velocity Doppler effect (Feldman and Drake, 1986). This effect is removed (Figure 13.3b) by normalizing both the 100 wt% WEH simulation results and the measurements to the no-water simulation values. The dominant remaining signal in the measured epithermal neutron data is a relative count-rate decrease versus latitude poleward of approximately latitude 70°N. The magnitude and latitude profile of this variation closely matches that of the simulated count rate for a thick, surficial layer of 100 wt% water ice at all of the radar-bright regions identified from radar observations (Harmon et al., 2011).

Given the highest-latitude value as the maximum polar signal, the epithermal neutron data show a measured polar signal of 0.976 ± 0.0025 (two standard deviations, or 2σ), relative to an equatorial neutron signal of 1. After accounting for remaining systematic variations due to background counts from energetic electron events and possible subsurface temperature variations,

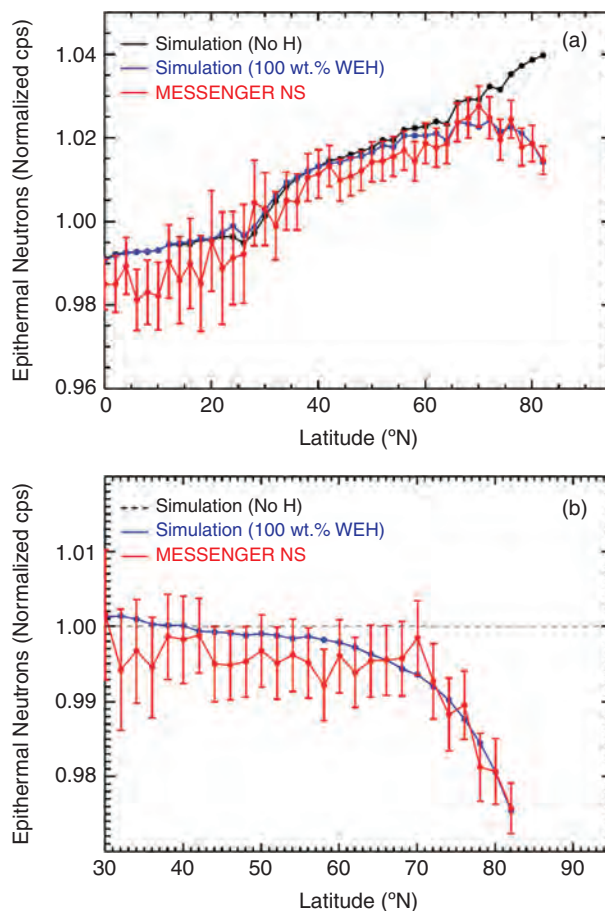


Figure 13.3. (a) Measured (red) and simulated (black, blue) epithermal neutron count rates averaged over 2°-wide latitude bins and plotted as a function of latitude. All corrections except for a radial Doppler effect have been applied to the data. Counts are normalized to the mean count rate (~60 counts per second, or cps) at an altitude of 400 km. Simulated count rates are shown for the cases of no hydrogen (black) and a thick layer of 100 wt% water-equivalent hydrogen (WEH) (blue) in the radar-bright regions. The error bars denote twice the measured standard deviation of the mean in each latitude bin. (b) Simulated and measured epithermal neutron count rates after correcting for the radial Doppler effect, which is accomplished by normalizing to the simulation with no hydrogen. From Lawrence et al. (2013).

Lawrence et al. (2013) concluded that the epithermal neutron data provide strong evidence that Mercury's north polar radar-bright regions contain high concentrations of hydrogen, consistent with the presence of water ice. If it is assumed that the water ice is located within the radar-bright regions as a single thick layer, then the epithermal neutron data are consistent with the presence of up to 100 wt% WEH within these regions. That the 2σ uncertainty of the measurements extends to a slightly larger signal than is given for the hydrogen-rich simulation indicates that the epithermal neutron data are consistent with (but do not require) a larger total area than is specified by regions identified as radar-bright by Harmon et al. (2011).

The NS also measured fast neutrons, which depend on hydrogen concentration, but with less sensitivity and diagnostic specificity than epithermal neutrons. Fast neutrons have a different sensitivity to hydrogen-rich material buried under tens of

centimeters of hydrogen-poor material than epithermal neutrons, and the combination of epithermal and fast neutron measurements can constrain the burial depth of a hydrogen-rich layer under a hydrogen-poor layer (Feldman et al., 2007; Miller et al., 2014). When the epithermal and fast neutron measurements are combined, the inferred polar hydrogen enhancements are consistent with an average two-layer stratigraphy in which the hydrogen concentration in the upper layer is 0–25 wt% WEH, the hydrogen concentration in the lower layer is 12–100 wt% WEH, and the effective surface density of the upper layer is 12–35 g/cm² (Lawrence et al., 2013). If a typical planetary regolith density of 1.5 g/cm³ is assumed (Carrier et al., 1991), this surface density corresponds to a physical thickness of 8–23 cm.

The results from radar and neutron observations give a consistent picture of the polar deposits. Specifically, the identification from neutron data of large concentrations of hydrogen within the radar-bright regions strongly supports the idea that the high radar backscatter of the polar deposits is the result of nearly pure water ice (Harmon et al., 2011). Multi-wavelength radar data also support the interpretation that the water-rich layer, on average, is buried beneath an insulating layer of ~10 cm thickness (Harmon et al., 2011). This thickness falls within the range 8–23 cm inferred from the neutron data. Finally, because the neutron simulations used the same locations of radar-bright features as MESSENGER illumination studies (Chabot et al., 2013; Deutsch et al., 2016; also Section 13.2.1), the combined results provide a self-consistent basis for interpreting the locations of hydrogen, permanent shadow, and radar-bright deposits.

13.2.3 Laser Reflectance Measurements

MESSENGER's Mercury Laser Altimeter (MLA) (Cavanaugh et al., 2007) obtained the first topographic measurements of Mercury's surface (Chapter 3), which contributed to identifying regions of permanent shadow near Mercury's north pole, as discussed in Section 13.2.1. Additionally, MLA measured the reflectance of the surface at the laser wavelength of 1064 nm, providing key new insights into Mercury's polar deposits.

The single-beam time-of-flight MLA ranging system measured the surface elevation at 8 Hz (~400-m intervals) as well as zero-phase reflectance at 1064-nm wavelength during much of the orbital mission. Brief (~6 ns) laser pulses with ~20–100-m-diameter footprints were reflected from the surface and collimated by four telescopes into a single detector photodiode, converted to an electronic signal, and amplified. As little as 0.1 fJ of detected return signal energy sufficed to make a range measurement. The laser output, range, and incidence and emission angles all affect the reflectance intensity, and to determine the surface reflectance all of these factors must be considered. The energy of the return pulse as a fraction of the outgoing laser pulse energy provides the reflectance, which is obtained by solving the lidar link equation:

$$E_{rx} = E_{tx} \eta_r \frac{A_{rx} r_s}{R^2 \pi}, \quad (13.1)$$

where E_{rx} is the received signal pulse energy, E_{tx} is the transmitted laser pulse energy, η_r is the receiver optics transmission at the laser wavelength, A_{rx} is the receiver telescope aperture area, R is the distance from the MESSENGER spacecraft to the illuminated surface, and r_s is the target surface reflectivity (relative to a Lambertian sphere, i.e., an ideal, diffusely reflecting surface). A narrow, 0.3-nm-wide transmission window rejects almost all background solar radiation. The energy of the outgoing pulse was measured directly after attenuation through the laser output turning mirror. In ground testing, the laser energy varied as a function of temperature from ~14 to 22 mJ and was recorded by the energy monitor with ~10% precision. The return pulse energy was inferred from the differential pulse width of detector signal triggers measured simultaneously at low- and high-voltage thresholds (Sun and Neumann, 2015). Although less precise than a direct measurement, the dual-threshold detection scheme maximized the range sensitivity and provided an estimate of pulse spreading as well. The detector electronics incorporated programmable gain and threshold settings that allowed operation nominally between 200 and 1500 km range. Under optimal conditions, the energy measurement had a 25% precision at one standard deviation. Ground calibration of detector parameters provided a conversion of electrical signal to energy. The MLA measurements could be made in complete darkness as well as sunlight and were virtually unaffected by background solar flux, but required near-nadir incidence to produce a suitable pulse. Off-nadir measurements generally involved ranging to longer distances, which resulted in the laser footprint being wider, its radiance being fainter, and the higher incidence angle combined with the slope of the terrain spreading the return signal energy over a longer interval than the response time associated with the detector circuit. Thus, off-nadir observations often resulted in signals too low to trigger both thresholds. Moreover, the steepest poleward-facing slopes are hidden from MLA measurements, and overall the MLA coverage was limited by spacecraft geometry. Detection of ground returns over steep slopes was aided by a matched filter design for the receiver, allowing detection of surface returns at high angles but without energy measurements. Over the steepest and darkest surfaces, the very few dual-threshold returns indicated a very low reflectance.

The north polar region was densely sampled by MLA at nadir incidence from altitudes of ~250 to 460 km over the course of four years and more than 4000 orbits. A map of the surface reflectance (Neumann et al., 2013; Deutsch et al., 2017a) in regions of high density and good signal determined from MESSENGER's full orbital data set is shown in Figure 13.4, which can be compared with the image mosaic in Figure 13.2. Reflectance measurements north of 84°N required off-nadir observations, due to the spacecraft's orbital inclination, and hence these measurements are noisier than the nadir observations at lower latitudes. Along with the reflectance measured off-nadir, the sampling at latitude >84°N was also sparse, resulting in an overall degradation of the data quality and an inability to determine precisely the reflectance contrast in this northernmost region.

Whereas Mercury's sunlit regolith in the north polar region has an average surface reflectivity value r_s of 0.17, it is apparent

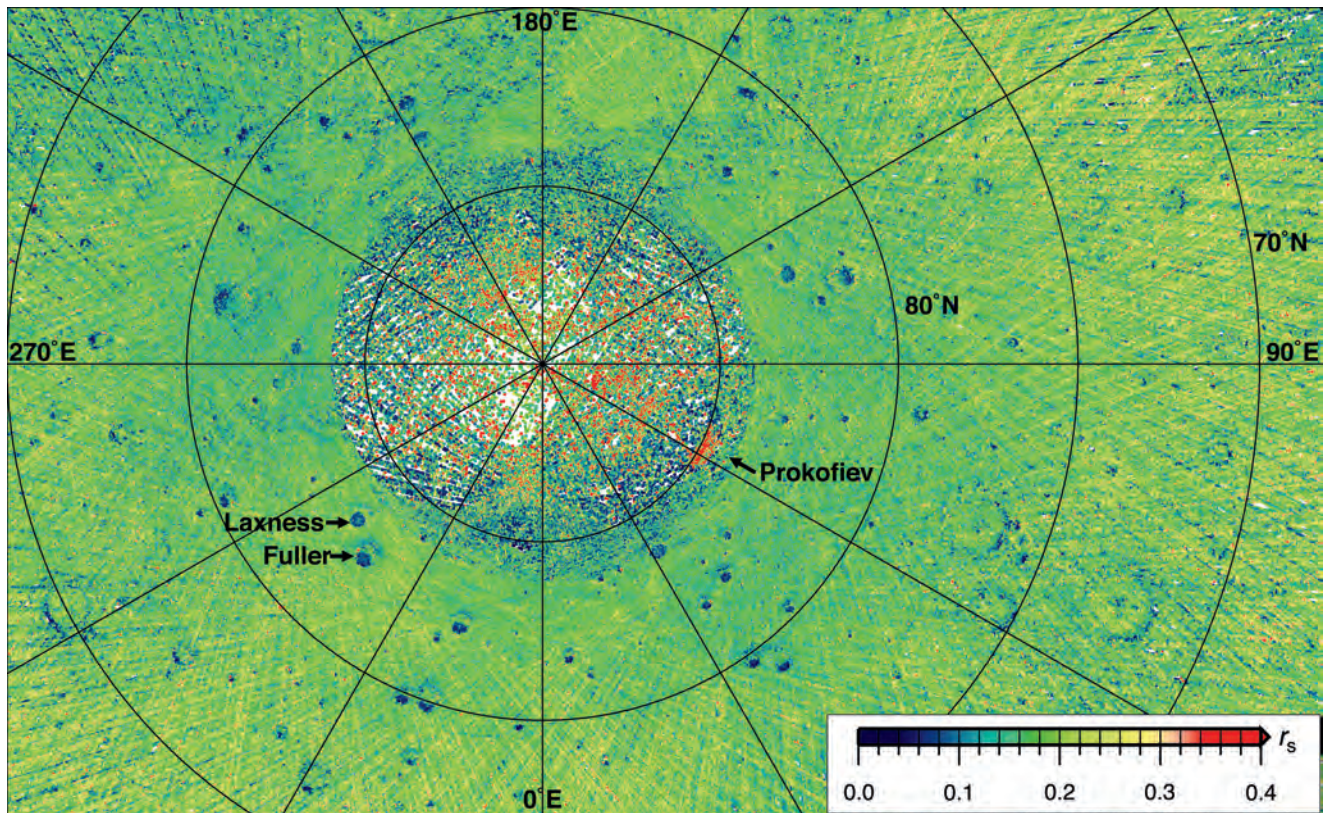


Figure 13.4. The bidirectional reflectance (r_s) of Mercury's north polar region at 1064-nm wavelength (Neumann et al., 2013; Deutsch et al., 2017a), median binned at 0.4-km resolution using nearest-neighbor interpolation. Lower reflectance values within many permanently shadowed craters, such as Laxness and Fuller, are evident, as are higher-reflectance regions, such as those within Prokofiev. The MLA reflectance measurements in regions poleward of Prokofiev were acquired at off-nadir viewing geometries and were more limited because of the spacecraft's orbital inclination.

from Figure 13.4 that the large majority of permanently shadowed surfaces within polar craters contain material with considerably lower reflectance ($r_s < 0.1$). The low-reflectance surfaces within the craters are preferentially located on poleward-facing slopes and are not found in regions that experience direct solar illumination. The lowest reflectance values represent only an upper bound, because such surfaces attenuate or extinguish laser returns to levels below the sensitivity of the detector. Neumann et al. (2013) noted that, where coverage was available, all radar-bright regions at latitudes $<84^\circ\text{N}$ have low-reflectance surfaces, a finding confirmed by subsequent MESSENGER MLA observations from the entire orbital mission.

Examples of craters with low-reflectance shadowed surfaces are shown in Figure 13.5 for Laxness and Fuller. Portions of these flat-floored, central-peak craters (Figure 13.5a) have regions of permanent shadow (Figure 13.5b) and high radar reflectivity (Figure 13.5c), and in these regions the reflectance is lower than in the surrounding illuminated areas (Figure 13.5d). The location of the low-reflectance boundary is not distinctly defined, but the low-reflectance surface includes the radar-bright region in Figure 13.5c and is generally consistent with the region of permanent shadow inferred from topography.

Low-reflectance surfaces are also found in many small, simple craters where pre-MESSENGER thermal models predicted that water ice could not be stable at the surface or near subsurface (Vasavada et al., 1999). The 6-km-diameter, bowl-shaped

crater near Laxness, labeled “L4” in Figure 13.5, is one such example. The poleward-facing interiors of many similarly sized craters, even some at latitudes south of 70°N , also have very low-reflectance signals as measured by MLA. Low-reflectance surfaces are found in permanently shadowed regions other than crater interiors, such as on the poleward-facing scarp at 83°N , 270°E , which crosses craters Qiu Ying and Bechet. Additionally, scattered areas on the northernmost flanks of some craters also have lower reflectance values in the MLA map, as is seen for Laxness and Fuller in Figure 13.5. These areas do not host large regions of permanent shadow, but it is possible that small shadowed regions, with dimensions below the spatial resolution of current shadow maps (Mazarico et al., 2014; Deutsch et al., 2016) or Arecibo observations (Harmon et al., 2011), are present, perhaps as a result of surface roughness and the limited sunlight that illuminates this location. In fact, a gradual poleward darkening of the surface from $\sim 72^\circ\text{N}$ to $\sim 85^\circ\text{N}$ in the MLA reflectance map has been attributed to the presence of low-reflectance volatile deposits in “micro-scale cold traps,” which are at spatial scales below those resolved by MLA (Paige et al., 2014; Neumann et al., 2017). Modeling suggests that surface roughness can result in an areal fraction for micro-scale cold traps of up to $\sim 20\%$ for Mercury's north polar region (Rubanenko et al., 2017).

In contrast to the low-reflectance surfaces identified within the majority of permanently shadowed craters, the permanently

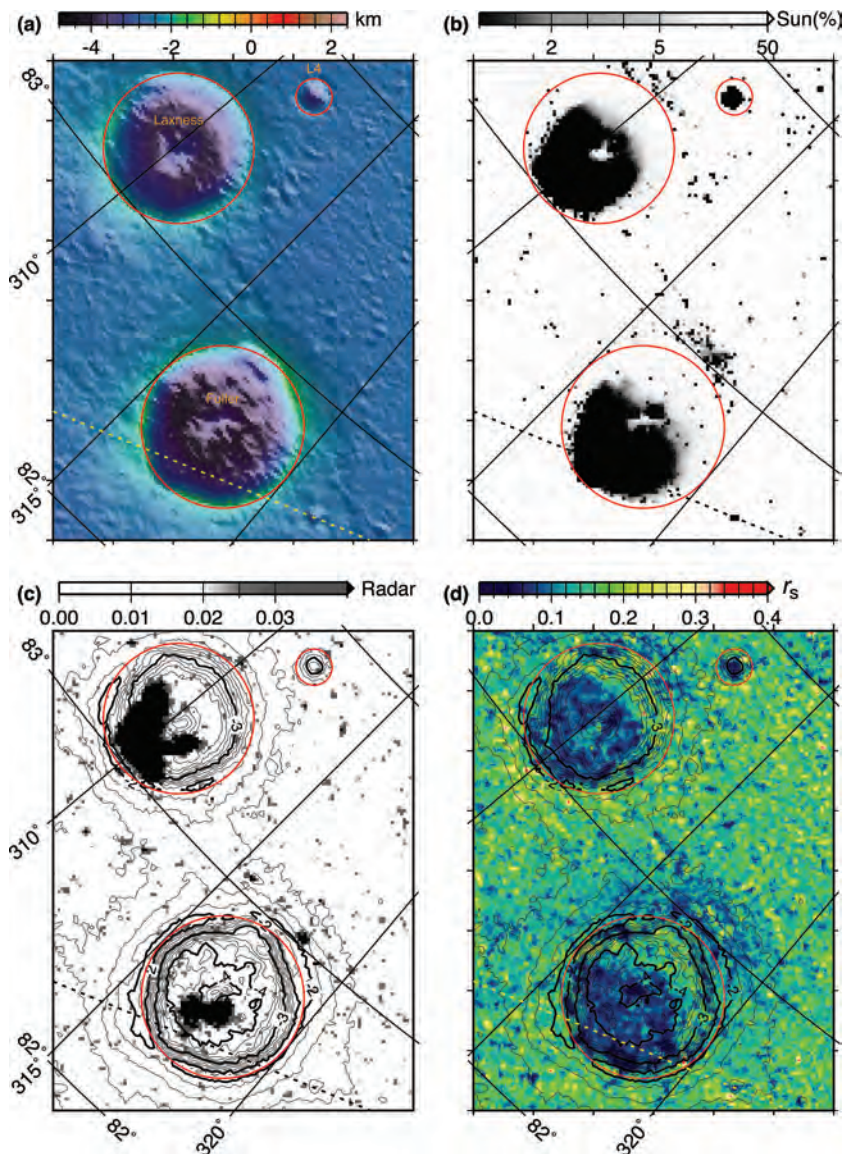


Figure 13.5. (a) MLA topography of complex craters Laxness (26-km diameter) and Fuller (27-km diameter) and a 6-km-diameter crater northeast of Laxness denoted L4. Red circles denote rim crests. Polar stereographic projection of height relative to a 2440-km-radius spherical datum. (b) Percentage of time illuminated by sunlight determined from MLA topography (Mazarico et al., 2014; Deutsch et al., 2016). (c) Radar reflectivity (Harmon et al., 2011). Contours of topography are shown at 0.2-km intervals. (d) MLA reflectance (r_s). Dashed lines show the location of the profile through Fuller in Figure 13.6.

shadowed interior of the 112-km-diameter Prokofiev crater contains an anomalously high-reflectance surface, as seen by the red area in Figure 13.4. During MESSENGER's second year of orbital operations, several MLA profiles were obtained with off-nadir targeting at modest incidence angles ($<10^\circ$) through Prokofiev, and these profiles showed areas of enhanced reflectance. The precise boundary of the high-reflectance region is not well resolved, but the average reflectance in this region is $r_s = 0.3$, unusually high for Mercury, and is interpreted as indicating a surface exposure of water ice (Neumann et al., 2013). The northernmost large craters, Kandinsky, Tolkien, Chesterton, and Tryggvadóttir (Figure 13.2), which have permanently shadowed interiors conducive to stable surface water ice (Paige et al., 2013; Section 13.2.4), also display evidence for high-reflectance surfaces (Deutsch et al., 2017a) but from more limited and scattered MLA reflectance data than Prokofiev, as seen in Figure 13.4. Additionally, four small but resolvable areas 2–5 km in diameter within 8° of Mercury's north pole

have been shown to exhibit clusters of high MLA reflectance values, consistent with the presence of surface ice exposed in small cold traps in these locations (Deutsch et al., 2017a). Overall, the MLA reflectance map shows an increase in the latitudinally averaged reflectance value from $\sim 85^\circ\text{N}$ to Mercury's north pole, interpreted to be the result of increasing amounts of surface water ice present in micro-scale cold traps (Neumann et al., 2017).

MLA topography and reflectance measurements for the low-reflectance surface observed in Fuller crater and the high-reflectance surface detected in Prokofiev crater are shown in Figure 13.6. As shown in Figure 13.6a for Fuller, the ~ 2 -km-deep crater wall on the left is too steep ($>27^\circ$ slope) for successful reflectance measurements, but the interior has reflectance values lower than the surrounding plains by a factor of at least 2. For Prokofiev (Figure 13.6b), the steeper walls of the crater have low reflectance, but the floor has much higher reflectance than the surroundings.

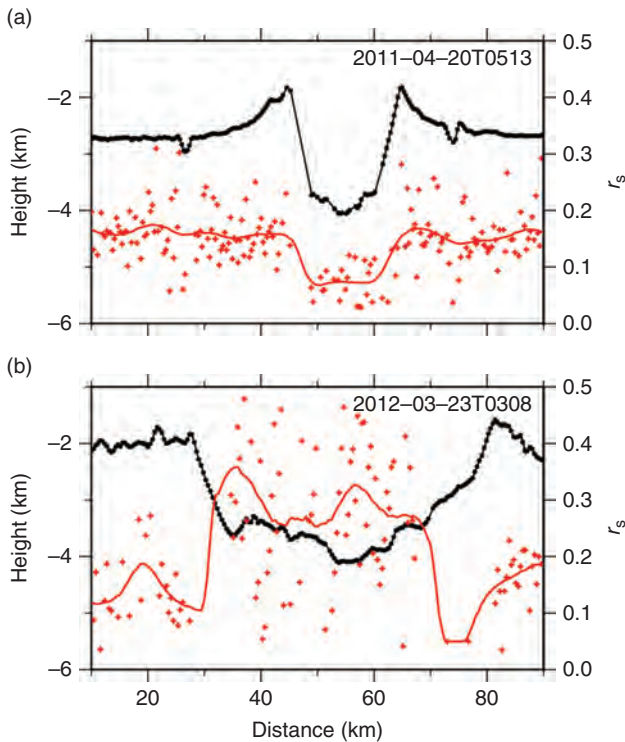


Figure 13.6. Profiles of MLA topography (black, labels at upper right), individual MLA reflectance measurements (red symbols), and reflectance averaged over a 12-km-wide cosine window (red curve). Surface height relative to a 2440-km-radius spherical datum is plotted with a 10:1 vertical exaggeration relative to the distance. (a) For Fuller crater, the profile location is shown in Figure 13.5. (b) For Prokofiev crater, the profile is taken along the 85°N latitude line.

13.2.4 Thermal Modeling Results

Measurements from MLA enabled major advances in constructing thermal models of Mercury's surface and near surface from the measured topography (Chapter 3). Previous thermal modeling work had necessarily relied on idealized crater shapes (Paige et al., 1992; Ingersoll et al., 1992; Salvail and Fanale, 1994; Vasavada et al., 1999). MESSENGER's MLA measurements led to the production of a digital elevation model that was used for thermal model calculations of Mercury's north polar region (Paige et al., 2013). The thermal model results were obtained from three-dimensional ray-tracing calculations that yielded surface and near-surface temperatures, as described by Paige et al. (2013), and were similar to thermal models determined earlier for the Moon (Paige et al., 2010). The resulting biannual maximum surface temperatures and biannual average temperatures at 2-cm depth are shown in Figure 13.7. Biannual maxima and averages are shown because it takes Mercury two orbits about the Sun to complete the full thermal cycle experienced by the planet. The results in Figure 13.7 are similar to those published by Paige et al. (2013) but generated from an MLA-derived DEM with more complete coverage than was available previously.

The thermal model results indicate that the maximum surface temperatures in large craters at high latitudes are sufficiently low to permit water ice deposits to be stable at the surface for

geologically long intervals (Figure 13.7c). The results suggest that substantial water ice may be expected on the surfaces of the interiors of craters Kandinsky, Tolkien, Chesterton, Tryggvadóttir, and Prokofiev (Figure 13.2), consistent with the observation of higher surface reflectance values measured by MLA in these permanently shadowed regions (Figure 13.4). However, the results also show that the majority of permanently shadowed craters near Mercury's north pole experience biannual maximum surface temperatures that are greater than ~ 110 K, values too high for water ice to be stable at the surface (Figure 13.7c).

On Mercury, biannual average temperatures can be interpreted as close approximations to the nearly constant subsurface temperatures that exist below the penetration depths of the diurnal temperature wave, which is tens of centimeters for a lunar-like regolith (Paige et al., 2013). Many permanently shadowed craters in Mercury's north polar region have average temperatures conducive to the thermal stability of subsurface water ice (Figure 13.7c), and these locations correlate with regions that are also radar-bright (Figure 13.7d). Conversely, regions with average temperatures higher than ~ 110 K are not observed to host substantial radar-bright deposits (Paige et al., 2013). This result suggests that the radar-bright deposits are dominantly composed of a volatile species that is not thermally stable at temperatures higher than 110 K, providing strong evidence for water ice as the major component of Mercury's polar deposits.

Additionally, in these locations conducive to the thermal stability of subsurface water ice, MLA measurements consistently have shown low-reflectance surfaces (Figure 13.4). Comparison of the MLA reflectance measurements with the thermal model results indicate that low-reflectance surfaces are absent in regions with biannual average temperatures greater than 210 K and biannual maximum temperatures greater than 300 K, leading to the conclusion that the distribution of low-reflectance substances must be controlled by the presence of volatile compounds that are not thermally stable above these temperatures (Paige et al., 2013). Combining the evidence for subsurface water ice with that for a low-reflectance layer of a higher volatility temperature, Paige et al. (2013) concluded that the low-reflectance deposits form as sublimation lags, eventually insulating the water ice below, similar to the earlier suggestion of Vasavada et al. (1999) that the ice deposits might sublimate until their contaminant load formed thin insulating layers. In such a scenario, a source of both water ice and low-reflectance volatiles is required, both of which migrate to the polar cold traps, leading to the suggestion that the low-reflectance volatiles, stable only below ~ 300 K, are organic-rich compounds derived from asteroidal or cometary impacts (Paige et al., 2013). Figure 13.8 (Zhang and Paige, 2009, 2010) illustrates that a range of organic compounds found in primitive meteorites (Botta and Bada, 2002), such as aromatic hydrocarbons, linear amides, and carboxylic acids, are potential compounds to consider for the identity of the low-reflectance layer covering most of Mercury's polar deposits.

One important issue to address with future thermal models is that of small simple craters. On the basis of pre-MESSENGER thermal models, derived for idealized bowl-shaped craters, it was concluded that simple craters on Mercury (<10 -km

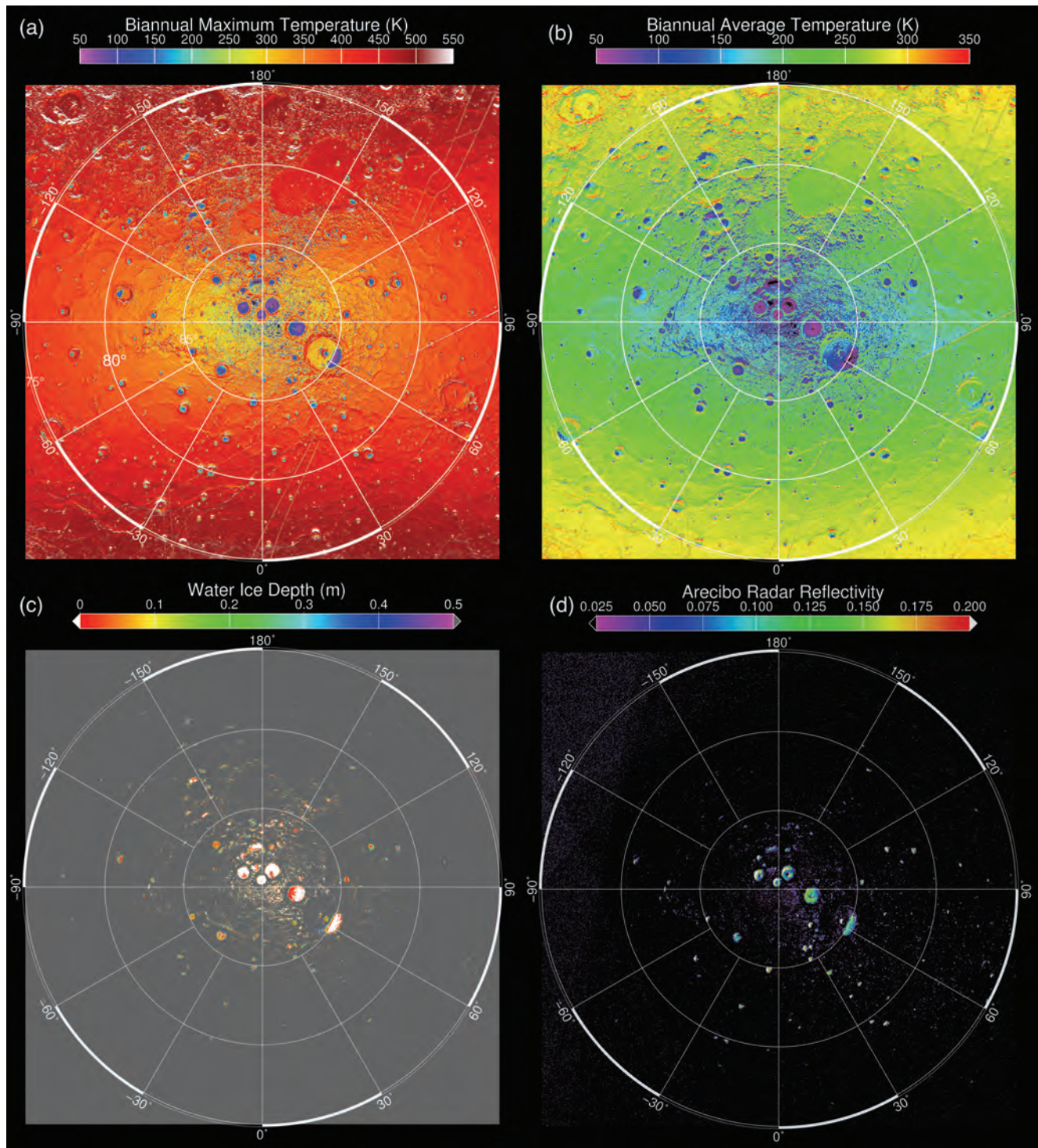


Figure 13.7. Results from thermal model calculations (Paige et al., 2013) for (a) biannual maximum surface temperatures and (b) biannual average surface temperatures at 2-cm depth for Mercury's north polar region. (c) Calculated depths at which water ice would be lost to sublimation at a rate of less than 1 kg m^{-2} per billion years given an insulating cover of lunar-like regolith; white regions indicate locations where water ice is thermally stable at the surface, and colored regions show the minimum depths at which water ice must be buried below the surface to be thermally stable. (d) Arecibo radar image from Harmon et al. (2011), to which the figure in (c) bears strong resemblance.

diameter) could not host long-lived water ice except if located within 2° of the pole (Vasavada et al., 1999). Yet mapping of radar-bright host craters (Section 13.2.1) indicates that many small craters contain radar-bright deposits, and MLA

measurements show these deposits to have low-reflectance surfaces (Figure 13.5, Section 13.2.3). Such craters are shallower (Ernst et al., 2014) than was assumed for the earlier thermal models. Thermal models based on MESSENGER

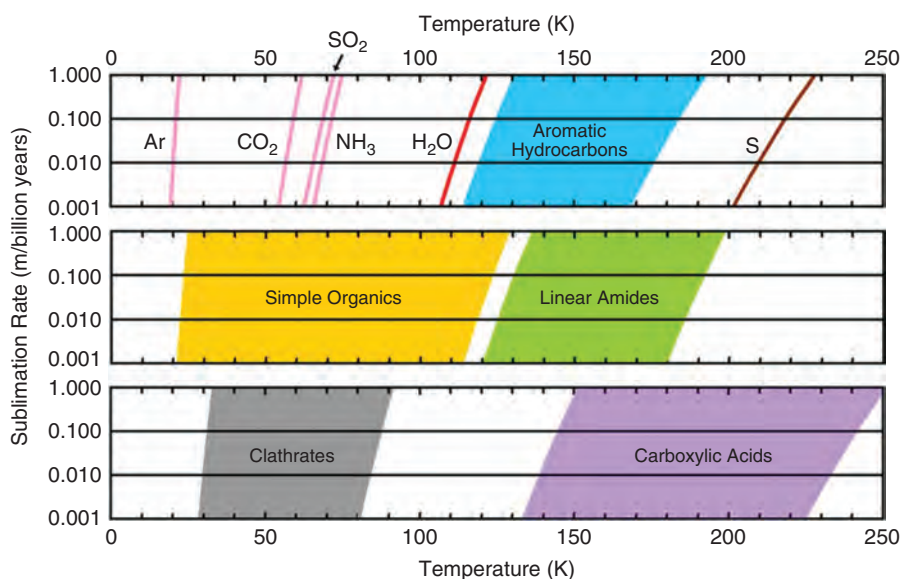


Figure 13.8. Shaded regions represent the range of vacuum evaporation rates calculated for representative organic compounds measured in primitive meteorites. Most simple organic compounds have volatility temperatures lower than that of water, but more complex organic compounds with higher molecular masses are stable to higher temperatures than water, consistent with the maximum surface temperatures calculated for Mercury's low-reflectance polar deposits. From Zhang and Paige (2009, 2010).

measurements of the topography of these small simple craters can yield insight into whether such craters can provide long-term stable environments for water ice or whether Mercury's water ice must be relatively young. Extending thermal models to cover the potentially challenging thermal environments experienced by the lowest-latitude craters that host radar-bright material, such as Egonu and Monk (Figure 13.2), could also provide insights into water ice stability on Mercury.

Currently, no thermal model calculations that include Mercury's surface topography have been performed for Mercury's south polar region, since MLA measurements were limited largely to Mercury's northern hemisphere. Studies with MDIS-derived DEMs, and suitable assumptions to deal with permanently shadowed surfaces within such DEMs, may yield thermal modeling results for Mercury's south polar region and enable comparison with the north polar results.

13.2.5 Direct Imaging of Polar Deposits

Directly imaging the permanently shadowed surfaces of radar-bright deposits was not a measurement objective of MESSENGER's one-year primary mission nor a required measurement for the MDIS instrument. However, as the spacecraft continued to operate and the mission was given extensions (Chapter 1), new measurement objectives were added, and one such addition was a campaign to image the surfaces of Mercury's polar deposits. Such observations are challenging, as the permanently shadowed surface is illuminated only by very low amounts of sunlight scattered off nearby terrain. Similar imaging had successfully revealed the permanently shadowed surfaces inside lunar craters (Haruyama et al., 2008; Speyerer and Robinson, 2013), indicating that attempts by MESSENGER might be successful. The MDIS WAC was equipped with 11 narrow-band filters (4–20-nm bandpasses) and one broadband clear filter (600-nm bandpass) centered at 700 nm (Hawkins et al., 2007). Designed with the main purpose of obtaining calibration images of stars, the WAC broadband

filter yielded images that quickly saturated when viewing Mercury's sunlit surface but provided high sensitivity to the low light levels necessary to image shadowed regions. To reveal details within shadowed areas, such regions had to be targeted on the edge of the WAC charge-coupled device (CCD) that was read out first, so that the low signal would not be compromised by saturation effects from the surrounding saturated terrain. With this approach, MESSENGER was able to image the radar-bright surfaces within a number of north polar craters; the spacecraft's highly eccentric orbit, with an altitude about 20 times higher above the south polar region than the north, did not enable a similar WAC broadband imaging campaign for Mercury's south polar radar-bright deposits.

The largest crater that hosts extensive radar-bright deposits in Mercury's north polar region is Prokofiev (112 km in diameter), the shadowed interior of which, as discussed above, exhibits evidence for surficial water ice, on the basis of high MLA reflectance measurements (Neumann et al., 2013) and thermal model predictions for water ice stability (Paige et al., 2013). Two WAC broadband images revealed that a portion of Prokofiev's floor has a higher reflectance than the surrounding surface (Chabot et al., 2014), as seen in Figure 13.9. The higher-reflectance surface is located in the portion of Prokofiev that hosts the large radar-bright deposit, consistent with surface water ice at this location. In the WAC broadband images, the higher-reflectance region has only 4–5% greater relative reflectance than the immediately neighboring surface, but the illumination conditions during these images are complicated: grazing sunlight at high solar incidence angles scatters off multiple surfaces, contributing to the combined illumination on each portion of the scene. Given the complex illumination conditions, the determination of absolute reflectance values from the WAC broadband images would require highly detailed modeling of the multiply scattered sunlight incident on each surface. In contrast, MLA measurements were obtained at a phase angle of zero and provided a more direct measurement of absolute reflectance values for regions within Prokofiev.

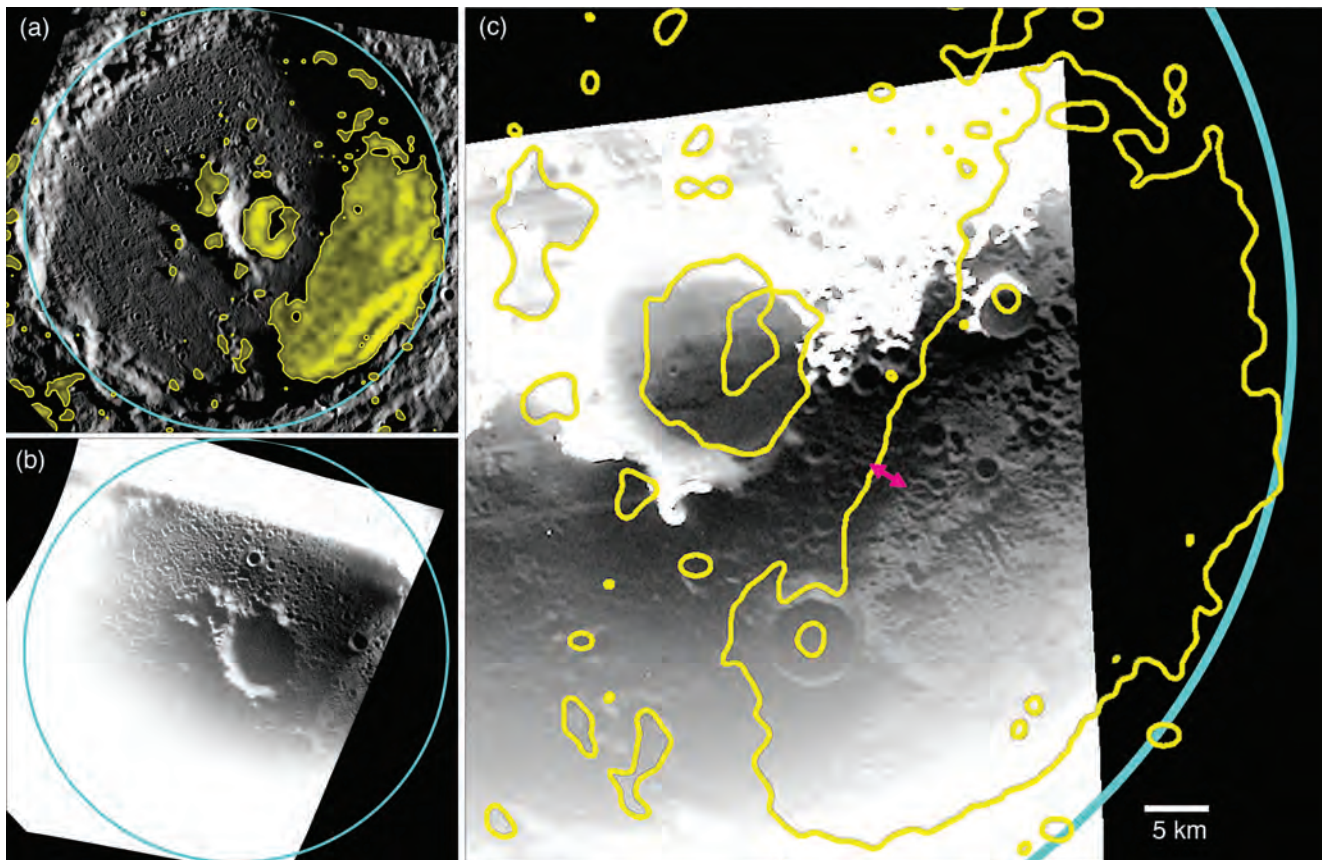


Figure 13.9. Prokofiev (112-km diameter) crater, with the rim outlined in cyan. All images are in stereographic projection about the north pole, with 180°E to the top. (a) Arecibo radar data are shown in yellow (Harmon et al., 2011); variations in radar backscatter across the permanently shadowed portion of the crater floor are related to topography. Two WAC broadband images, (b) EW1020581108B and (c) EW1019169411B, for which sunlit portions are saturated, reveal a higher-reflectance surface for the permanently shadowed, radar-bright region (Chabot et al., 2014). The pink arrows denote the approximately 3-km offset between the outer boundaries of the radar-bright region and the higher-reflectance surface.

Such measurements indicate that the geometric albedo within the radar-bright region of Prokofiev is approximately a factor of 2 higher than Mercury's average surface value at the near-infrared wavelength of the laser (Neumann et al., 2013).

The WAC broadband images also reveal the surface texture of the radar-bright region in Prokofiev. At the 85 m/pixel scale of the images, the surface texture appears similar to that seen on the neighboring portions of the crater floor that regularly receive direct solar illumination. This result indicates that if the higher-reflectance region is water ice exposed at the surface, its thickness does not noticeably affect the texture of the surface at this scale. In particular, the water ice is not sufficiently thick to make the covered surface appear smoother than the uncovered surface at 85 m/pixel. Small craters dominate the surface within Prokofiev, and yet the higher-reflectance region is fairly uniform in its surface reflectance properties. The images do not show evidence that higher-reflectance material is covered in local regions by ejecta from any of the small craters widely distributed across the floor of Prokofiev. This observation suggests that the higher-reflectance material in Prokofiev was emplaced after the small craters formed.

The higher-reflectance region in Prokofiev identified in the WAC broadband images is located within but is slightly smaller than the radar-bright region, as seen in Figure 13.9c. The higher-

reflectance surface is offset inward by ~3 km relative to the boundary of the radar-bright deposit, and the intervening ~3-km-wide region has a relative reflectance that is not distinguishable from the portions of Prokofiev's floor that receive direct solar illumination. Studies of mare–highland contacts on the Moon indicate that impact gardening has achieved lateral transport over a scale of ~4–5 km (Li and Mustard, 2000), a scale comparable to the difference in boundary position between the higher-reflectance and the radar-bright regions in Prokofiev. Lateral mixing at lunar mare–highland contacts has operated over billions of years. It is possible that the higher frequency and generally higher velocity of impacts at Mercury relative to the Moon (Cintala, 1992; Borin et al., 2009, 2016) or a sufficiently thin deposit within Prokofiev could yield similar lateral transport effects on a shorter timescale. In general, if the ~3-km offset boundary between the higher-reflectance and radar-bright regions in Prokofiev is the result of lateral mixing having covered the outermost edge of surface ice with regolith, the emplacement of the water ice occurred sufficiently far in the past to allow the effects of lateral transport to develop undisturbed. Alternatively, the thermal environment in Prokofiev may support a large area of surface ice surrounded by a marginal zone of subsurface ice, which is a general pattern often predicted in thermal models (Paige et al., 2010, 2013). Up to now, thermal

models have focused on global studies of Mercury's entire north polar region (Paige et al., 2013), and the precise region of permanent shadow within Prokofiev has not been determined with sufficient accuracy to address this offset region (Deutsch et al., 2016). A higher-resolution, localized study of the topography and thermal conditions in the Prokofiev region, at a scale approaching that of the WAC broadband images, would provide information key to interpreting the 3-km offset observed between the higher-reflectance and radar-bright regions.

WAC broadband images were also obtained of the radar-bright, permanently shadowed interiors of the four largest craters nearest Mercury's north pole: Chesterton, Kandinsky, Tolkien, and Tryggvadóttir (Figure 13.2). Although thermal models predict that these four craters, like Prokofiev, are capable of sustaining long-lived water ice at the surface (Figure 13.7c), the WAC broadband images showed that the floors of these craters do not look atypical for Mercury, and, in contrast to Prokofiev, no clear regions of differing reflectance properties were noted (Chabot et al., 2014). However, unlike Prokofiev, the entire floors of these high-latitude craters are in permanent shadow, so clear reflectance boundaries across their floors are not expected. Thus, the current analysis of the WAC broadband images of these four craters neither supports nor negates the possibility that water ice is exposed at the surface in these locations.

In contrast to Prokofiev and the few other large craters nearest Mercury's north pole, the polar deposits in the large majority of host craters have low-reflectance surfaces as measured by MLA at 1064 nm (Neumann et al., 2013) and are predicted to sustain long-lived water ice only if covered by an insulating layer a few tens of centimeters in thickness (Paige et al., 2013). As discussed above, this evidence has led to the interpretation that the insulating layer is a lag deposit composed of low-reflectance, cold-trapped, organic-rich volatile compounds stable at temperatures somewhat higher than water ice (Figure 13.8). WAC broadband images were acquired for many of these lower-latitude craters and, in total, reveal numerous examples of radar-bright locations with low-reflectance surfaces (Chabot et al., 2014, 2016). In the images, the low-reflectance surfaces are ~20% lower in relative reflectance than the nearby crater floor, but, as discussed for Prokofiev, the complex illumination conditions during these images complicates any determination of absolute reflectance values. The zero-phase-angle MLA reflectance measurements are better suited to provide this information and indicate that the low-reflectance deposits are approximately a factor of 2 lower in reflectance than Mercury's average surface (Neumann et al., 2013).

The best images of low-reflectance, radar-bright deposits were obtained during the final year of MESSENGER's orbital operations, when data were acquired at lower altitudes than in prior years (Chapter 1). The low altitudes enabled data sets of progressively higher spatial resolution for many instruments, including WAC broadband imaging within Mercury's shadowed polar craters. The low-altitude imaging opportunities were limited in area, however, and did not enable higher-resolution imaging within Prokofiev or other high-latitude craters. However, WAC broadband images were acquired of lower-latitude craters at resolutions as good as 24 m/pixel (Chabot et al., 2016), with examples shown in Figure 13.10.

A striking feature observed in the WAC broadband images of the low-reflectance deposits is the sharpness of the boundaries. These well-defined boundaries of the low-reflectance deposits align extremely closely with the boundaries of the permanently shadowed regions. In many cases, the boundaries of the radar-bright deposits are also similar, but in some locations, such as at Fuller crater, Arecibo radar data do not indicate an extensive radar-bright signal in the crater (Figure 13.2), but the crater shows a sizable low-reflectance deposit (Figure 13.10a). Though an absence of ice in such craters is one possibility, viewing or detection limitations of the radar observations can also affect the completeness of the identification of radar-bright features in Arecibo images. In fact, all of the 35 distinct craters with permanently shadowed surfaces revealed during the low-altitude imaging campaign show low-reflectance surfaces with well-defined boundaries (Chabot et al., 2016). This observation supports the suggestion that all of Mercury's available cold traps are occupied by volatiles. The well-defined boundaries of the low-reflectance deposits are not confined to topographic lows. To the contrary, the low-reflectance boundaries shown in Figure 13.10 extend up crater walls to just below the rim, notwithstanding that elsewhere on Mercury relatively bright material can be exposed on crater walls by slumping. Transects of relative surface brightness across the boundaries of the low-reflectance deposits show a transition zone approximately 400-m wide with intermediate brightness values (Chabot et al., 2016). This transition zone could be due to mixing between the low-reflectance compounds and regolith, or it could be due to variations in the amount of sunlit and permanently shadowed areas in this region on a scale smaller than the spatial resolution of the images.

If impact gardening of a low-reflectance deposit tens of centimeters thick exposed or thermally disturbed an underlying layer of water ice, any water ice exposed at the surface would quickly sublimate (1 m in 1 Myr at 130 K, and 1 m in 1000 yr at 150 K; Vasavada et al., 1999; Paige et al., 2013). While rapidly restoring the disturbed region to a stable configuration, new lag deposits of low-reflectance compounds would likely be formed, and this ongoing process could continually maintain well-defined boundaries. Such a process would not be active in colder permanently shadowed regions where water ice is stable at the surface, such as in Prokofiev, and hence it might account for the difference between the 3-km offset of the boundaries between the higher-reflectance region and the radar-bright material in Prokofiev and the sharp boundaries of the low-reflectance deposits in other craters. Regardless of the precise process, the well-defined boundaries of the low-reflectance deposits, even when imaged at resolutions of tens of meters, support the conclusion that the low-reflectance deposits are geologically young relative to the timescale for lateral mixing by impacts. This inference points either to delivery of volatiles to Mercury in the geologically recent past or to an ongoing process that restores the deposits and maintains sharp boundaries.

From the first WAC broadband images to resolve the low-reflectance deposits, Chabot et al. (2014) concluded that the reflectance of the deposits appeared uniform rather than patchy. However, subsequent higher-resolution WAC broadband images revealed that the low-reflectance deposits do display variations in brightness, such as seen in the example images of

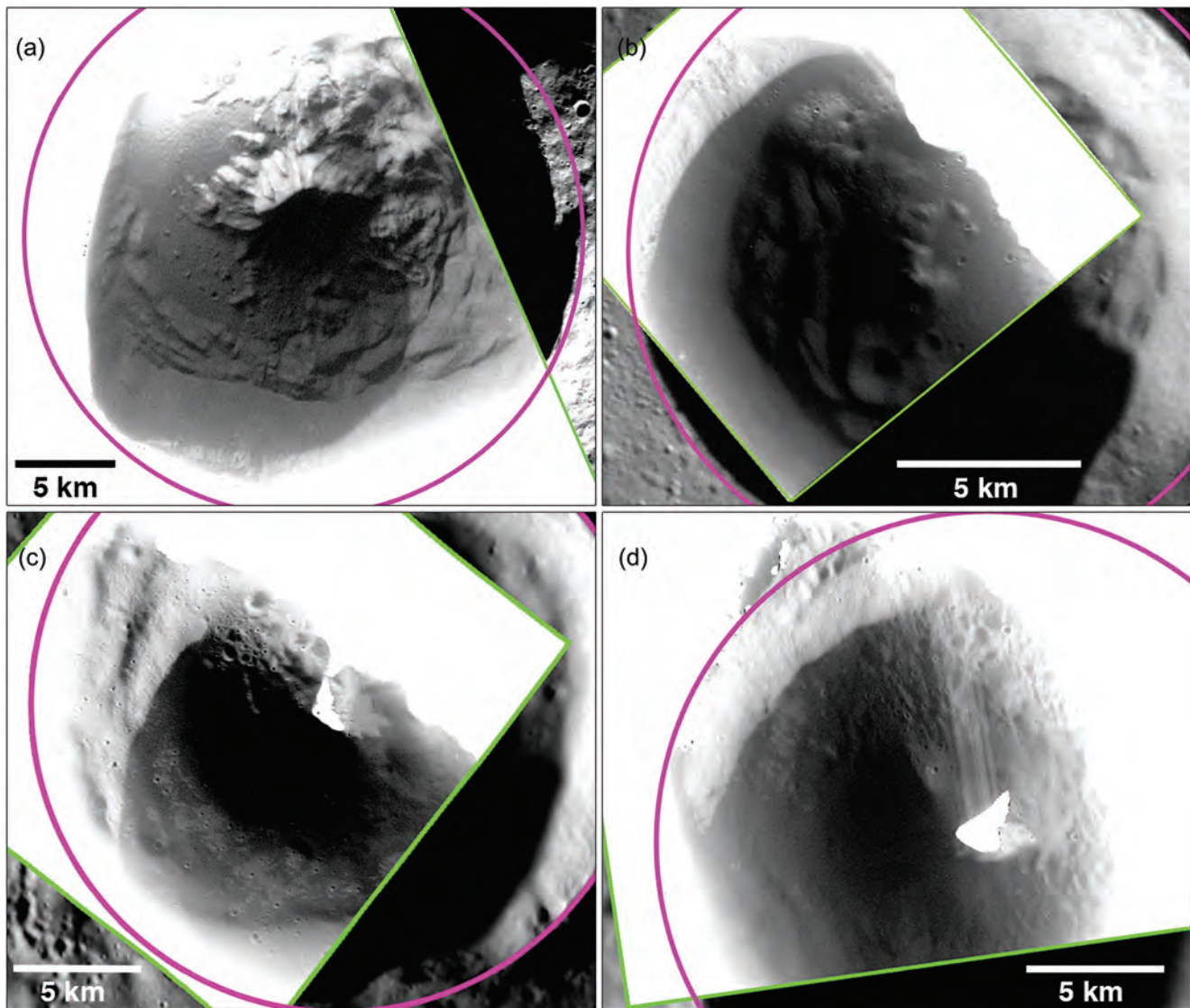


Figure 13.10. MDIS WAC broadband images, outlined in green, of Mercury's low-reflectance polar deposits (Chabot et al., 2016). Crater rims are outlined in magenta. All images are in stereographic projection about the north pole, with 180°E to the top. (a) Fuller crater (27-km diameter, 82.63°N, 317.35°E, EW1047206595B). (b) Unnamed crater at 80.30°N, 293.47°E (18-km diameter, EW1068017709B). (c) Ensor crater (25-km diameter, 82.32°N, 342.47°E, EW1051458815B). (d) Laxness crater (26-km diameter, 83.27°N, 309.96°E, EW1052529039B).

Ensor and Laxness in Figures 13.10c and 13.10d. In some craters, these brightness variations are correlated with variations in the modeled biannual maximum surface temperature, suggesting that the brightness variations are thermally controlled (Chabot et al., 2016). Control of surface reflectance variations by temperature could be the result of multiple volatile species that differ in reflectance and are stable to different maximum temperatures, implying the presence of multiple low-reflectance volatile compounds within Mercury's polar deposits. In contrast, in other craters, some of the small-scale brightness variations look as if they could be related to small impact craters that have disturbed the surfaces of the low-reflectance regions (Chabot et al., 2016), and such an observation may be inconsistent with these deposits being geologically young, as suggested by their well-defined boundaries. Higher-resolution

localized topography and thermal modeling studies of these craters could provide additional insights for interpreting the evolution of the low-reflectance deposits.

13.3 IMPLICATIONS

13.3.1 Evaluation of Pre-MESSENGER Hypotheses

Measurements and observations by multiple MESSENGER instruments, specifically NS, MLA, and MDIS, have greatly increased our knowledge about Mercury's polar deposits. These new data sets, combined with the Earth-based radar observations and thermal modeling results, enable an evaluation of previously proposed hypotheses for the composition of the polar deposits.

One proposed hypothesis was that Mercury's polar deposits are composed largely of elemental sulfur (Sprague et al., 1995). Sprague et al. (1995) preferred sulfur rather than water ice as the material in Mercury's polar deposits because of its stability to slightly higher temperatures and because there were good reasons to expect a sufficient abundance of sulfur at Mercury. Indeed, once MESSENGER entered orbit about Mercury and obtained compositional measurements of the surface, a high level of 1–4 wt% sulfur was discovered (Nittler et al., 2011). Although sulfur is now confirmed to be present on Mercury's surface, there is no quantitative study showing that a layer of elemental sulfur would create the high reflectivity and circular polarization ratio measured by the Earth-based radar observations, such as modeled by Black et al. (2001) for water ice on the Galilean satellites. Further, the complete sublimation of a 1-m-thick deposit of elemental sulfur over 1 Gyr would require a surface temperature of ~220 K, which is considerably higher than the corresponding ~110 K temperature for water ice (Vasavada et al., 1999). Whereas the higher stability temperature could support long-lived deposits even in the higher temperatures experienced within small simple craters (Vasavada et al., 1999), it also supports a polar cap of elemental sulfur exposed at the surface within 1° latitude of the pole and buried beneath the surface within 4° latitude of the pole (Butler, 1997; Vasavada et al., 1999). Neither Earth-based radar observations nor MESSENGER data sets support the existence of such an exposed or buried polar cap at either Mercury's north or south poles, however. In particular, the radar-bright regions identified from the highest-resolution radar images (Harmon et al., 2011) collocate with permanently shadowed regions even very near the pole (Figures 13.1 and 13.2), suggesting that the volatiles that compose the polar deposits require the colder thermal environments provided by the permanently shadowed regions. Additionally, MESSENGER's discovery of high-reflectance surfaces within craters that thermally can support long-lived water ice at the surface but low-reflectance surfaces for craters whose temperatures require water ice to be buried to be stable (Figures 13.4 and 13.7) indicates a transition temperature for the volatile material that is consistent with that of water ice but not with the higher stability temperature of sulfur. Lastly, MESSENGER's detection of enhanced hydrogen in Mercury's north polar region (Figure 13.3) is strong evidence that water ice is the dominant volatile in Mercury's polar deposits; polar deposits of sulfur provide no explanation for the enhanced polar hydrogen measured by MESSENGER.

Another hypothesis proposed for Mercury's radar-bright materials is that the high-radar-backscatter signals originate from the altered dielectric properties of silicates by very low temperatures (Starukhina, 2001). Although this hypothesis is consistent with the fact that the radar-bright materials are found in locations that experience the lowest temperatures on Mercury, it is not the best explanation for other observations. For example, the permanently shadowed regions of the Moon, which are even colder than those on Mercury (Paige et al., 2010), lack similar strong radar-backscatter signals, though this difference has been suggested as due to the different silicate compositions of the two bodies (Starukhina, 2001). However, the altered-dielectric-properties hypothesis does not offer an explanation for the high-reflectance and low-reflectance surfaces measured in the radar-bright regions

by the MLA and MDIS instruments. Finally, enhanced polar hydrogen abundances are not predicted by the altered-dielectric-properties hypothesis, as this hypothesis predicts no compositional difference between neighboring radar-bright and non-radar-bright surfaces.

The original hypothesis put forward to explain the first radar detections (Slade et al., 1992; Harmon and Slade, 1992; Butler et al., 1993) was that Mercury's polar deposits are dominantly composed of water ice, and multiple MESSENGER observations now provide further support for this interpretation. The enhanced hydrogen abundance measured in Mercury's north polar region by MESSENGER's NS is strong evidence for the presence of water ice (Lawrence et al., 2013). The determination that radar-bright deposits in both Mercury's north and south polar regions lie within regions of permanent shadow (Chabot et al., 2012, 2013; Mazarico et al., 2014; Deutsch et al., 2016) is consistent with the prediction of the water ice hypothesis. Thermal modeling with the MESSENGER-determined topography of Mercury's north polar region shows that the permanently shadowed regions have temperatures conducive to the long-lived stability of water ice deposits, either at the surface or in the near subsurface (Paige et al., 2013). Additionally, in regions where thermal models predict that surface water ice would be stable, higher reflectance surfaces are observed by both active near-infrared reflectance measurements by MLA (Neumann et al., 2013; Deutsch et al., 2017a) and visible-wavelength imaging by MDIS (Chabot et al., 2014) and are interpreted as evidence for water ice exposed at the surface. In regions where the thermal models predict that water ice is stable only if buried a few tens of centimeters below the surface, the same measurements reveal low-reflectance surfaces, interpreted to be a thin covering of volatile, organic-rich material that developed as a sublimation lag deposit and that insulates the water ice beneath it. Thus, the body of evidence from Earth-based radar and MESSENGER observations provide complementary and compelling evidence to answer MESSENGER's major science question: "What are the radar-reflective materials at Mercury's poles?" Mercury's polar deposits are dominantly composed of water ice.

13.3.2 Constraints on the Source of Mercury's Polar Water Ice Deposits

MESSENGER's observations of Mercury's polar deposits provide more than just evidence that the deposits are composed of water ice. Data from MESSENGER also yield new insights into the source, and hence the age and evolution, of water ice on Mercury and the history of volatiles in the inner solar system. Below are four key constraints, followed by discussion of the implications and consideration of the possible sources of Mercury's polar water ice deposits.

13.3.2.1 Constraints

(1) Mercury's Polar Deposits Are Dominantly but Not Solely Water Ice

One of the key new insights obtained from MESSENGER data is that although Mercury's polar deposits are dominantly water ice, they also contain other volatile materials. Although there

are no measurements of the composition of these other volatiles, they are thought to be the key constituents of the low-reflectance insulating layer observed in permanently shadowed regions that have surface temperatures greater than ~110 K, where surface water ice is not stable. The surfaces of this material have very low reflectance values, approximately half that of Mercury's normal regolith surface as measured by MLA at 1064 nm (Neumann et al., 2013), and surface brightness variations suggest the presence of multiple low-reflectance compounds in the deposits (Chabot et al., 2016). The low-reflectance surfaces are located only in permanently shadowed regions, suggesting that the low-reflectance layer is not stable in environments with maximum temperatures exceeding ~300 K. These combined observations support the hypothesis that the low-reflectance layers are composed of carbon-rich materials that have low reflectance values, and, while volatile, are stable to higher temperatures than water ice (Paige et al., 2013). Organic compounds vary widely in their volatilities, but those that are stable to sublimation at higher temperatures than water ice are complex and have high molecular weights, in contrast with most simple organic compounds, which are more volatile than water (Figure 13.8; Zhang and Paige, 2009, 2010). Such complex organic molecules are found in primitive meteorites (Botta and Bada, 2002), leading Zhang and Paige (2009, 2010) to suggest that if such materials were found in the polar cold traps on Mercury or the Moon, an impact origin for their source would be implied. The formation of higher-order organic compounds in Mercury's polar deposits through the chemical processing of simple ices by energetic magnetospheric particles, GCRs, and other sources has also been suggested (Crites et al., 2013; Delitsky et al., 2017). Paige et al. (2013) proposed that the low-reflectance layers could have formed rapidly after an impact on Mercury delivered both water and organic compounds to cold traps in the same permanently shaded locations. Subsequent evolution of these cold traps would have favored the sublimation of near-surface water ice, leaving a surface lag of complex organic material having higher volatility temperature and lower reflectance. Simulations of large impact events suggest that most of this organic material would be destroyed during the impact, but some fraction may survive, depending on impact conditions (Pierazzo and Chyba, 1999, 2006), though such simulations have not yet been specifically conducted for Mercury.

The presence of volatile materials other than water ice is an important constraint on the source of Mercury's polar deposits. If Mercury's water were predominantly formed by interaction of surface regolith with protons from the solar wind, such interactions would produce OH or H₂O but the production of other volatiles is not predicted (McCord et al., 2011).

Outgassing of volatile materials from Mercury's interior is also an option for the source of Mercury's polar deposits. MESSENGER found considerable evidence for past volcanic activity on Mercury, including features interpreted as vents surrounded by pyroclastic deposits interpreted to be the product of explosive volcanic eruptions driven by exsolution of volatiles in ascending magma (Chapter 11). Additionally, MESSENGER determined that Mercury is not depleted in volatile elements, with both sulfur and carbon measured on

the surface (Chapter 2). Graphite and amorphous carbon are not volatile but rather stable at temperatures across Mercury's surface (Bruck Syal et al., 2015), whereas the volatility temperatures of CO₂ and SO₂ are lower than that of H₂O, as are those of simple C-bearing molecules (Figure 13.8; Zhang and Paige, 2009, 2010). Hence, such materials cannot account for the low-reflectance surfaces observed on Mercury's polar deposits. However, elemental S is volatile but also stable to a higher temperature, as noted by Sprague et al. (1995) and shown on Figure 13.8, generally consistent with the biannual maximum surface temperatures experienced by the low-reflectance deposits.

Although indirect evidence supports the inference that the low-reflectance volatiles are organic compounds, determining the chemical and molecular composition of the low-reflectance volatile material would resolve this question and provide critical information on the source and evolution of Mercury's water ice deposits.

(2) Mercury's Polar Deposits Have Distinct Surface Reflectance Values and Sharp Boundaries

Another key new observation from MESSENGER about Mercury's polar deposits is that the surfaces of the deposits have distinctive reflectance characteristics that differ from the rest of Mercury's surface. The existence of these reflectance differences, and the fact that regolith gardening or other processes have not destroyed them, provides a constraint on the age of the deposits. Crider and Killen (2005) modeled the burial of water ice on Mercury through regolith emplacement and concluded that 20 cm of regolith would cover the water ice deposits in <50 Myr if water ice is lost from Mercury's surface by meteoroid impacts. Whereas migration simulations suggest that 98% of water molecules in polar cold traps are likely to recondense in those traps if disturbed (Butler et al., 1993), rendering the specific age estimated by Crider and Killen (2005) uncertain, MESSENGER observations indicate that Mercury's polar deposits are not dominantly buried by regolith but rather by material lower in reflectance than normal regolith, and the low-reflectance deposits show well-defined boundaries (Figure 13.10). The preservation of these distinctive reflectance properties and sharp boundaries indicates a geologically young age for the deposits.

The purity of the water ice exposed on the floor of Prokofiev is not known, but laboratory studies indicate that, depending on the ice particle size and viewing conditions, ice concentrations less than ~50% do not provide strong effects on the reflectance at visible to near-infrared wavelengths (Yoldi et al., 2015). Thus, since MLA zero-phase-angle observations and MDIS high-phase-angle imaging were both able to detect the higher-reflectance surface within Prokofiev, the majority of the surface must be composed of exposed water ice, placing a limit on the silicate regolith mixed into the region. Additionally, the temperatures within Prokofiev are sufficiently low that water molecules have very little diffusive mobility, and hence a diffusion process cannot account for the high-reflectance surface (Paige et al., 2013).

Other processes that would alter the water ice deposits on Mercury have also been proposed, including destruction by Lyman alpha photodissociation (Morgan and Shemansky,

1991), organic synthesis within ice bombarded by GCRs and solar energetic particles (Crites et al., 2013; Delistky et al., 2017), and chemical reactions induced by magnetospheric charged particles funneled onto Mercury's surface at high latitudes that could produce organic compounds and dark refractory materials in the ice (Delistky et al., 2017). Of these potential energy inputs that might initiate chemical reactions in Mercury's polar ices to yield new heavier-molecular-weight organic products, Delistky et al. (2017) concluded that magnetospheric particle energy deposition is two or more orders of magnitude greater than each of the other potential energy sources. However, the fact that Mercury has polar deposits with both higher-reflectance surfaces, such as in Prokofiev (Figure 13.9), and lower-reflectance surfaces, such as shown in Figure 13.10, argues against the idea that the surface reflectance of the deposits is produced dominantly by a weathering or alteration process, which would be expected to affect all of Mercury's polar deposits in a relatively uniform manner. Instead, the well-preserved surface reflectance properties, with both high- and low-reflectance surfaces, and the sharp boundaries of the polar deposits suggest that they are geologically young. The implication for the source of the water ice is that the material was either recently delivered to the planet or is actively refreshed and maintained, either from external sources or local redistribution.

(3) Mercury's Polar Deposits Are Relatively Pure and Extensive

The conclusion that Mercury's polar deposits are relatively pure water ice is not a new inference, but it remains an important constraint on the source, age, and evolution of water ice on Mercury. Radar observations of materials with a high circular polarization ratio and high radar reflectivity are indicative of icy materials on other solar system objects. Such deposits produce coherent backscatter effects from the essentially transparent nature of ice at radar wavelengths that results in multiple volume scattering with little radar energy absorption (Hapke, 1990; Hapke and Blewett, 1991). The volume scattering occurs from variations in density, which can be caused by silicate inclusions or fractures and voids. However, calculations indicate that to match the observed radar properties from Mercury's north polar region, even a small volume fraction of silicates mixed with the ice would contribute substantial absorption, leading to the conclusion that the ice in Mercury's polar deposits must be nearly pure, estimated at less than ~5% silicates by volume (Butler et al., 1993). The high radar reflectivity and circular polarization ratio have been observed at radar wavelengths of 3.5, 12.6, and 70 cm. If many multiple scatterings are required to yield the bright radar returns, then the scattering layer must be many wavelengths thick, implying that the ice has a minimum thickness of several meters (Black et al., 2010). However, the maximum possible thickness of Mercury's water ice deposits is poorly constrained by radar or MESSENGER observations and has been estimated to range from a few hundreds of meters to tens of meters or less (Section 13.2.1).

That Mercury's extensive water ice is relatively pure has also been interpreted to suggest that the water ice was likely deposited over a relatively short time period, because silicate particles would otherwise be present in larger amounts within the deposits (Butler et al., 1993). An episodic source, such as the impact

of a large comet or asteroid, is favored by such an argument, rather than a more nearly continuous source for Mercury's water ice. More continuous sources, such as sustained planetary outgassing or micrometeoroid delivery, are less likely to build up relatively pure water ice deposits, given that regolith gardening processes operate concurrently. However, the ability to produce pure water ice deposits would depend on the specific rates for all processes involved in the evolution of the deposits. Specific models that examine quantitatively the purity of water ice deposits that could be produced by micrometeoroid impacts or planetary outgassing on Mercury have yet to be developed. Improved constraints on the thickness of the water ice deposits and their purity could also provide limits on the total volume of material delivered and the timing of its emplacement.

(4) Polar Deposits Similar to Those on Mercury Are Not Seen on the Moon

The Moon, like Mercury, has regions of permanent shadow near its poles (Bussey et al., 1999, 2005, 2010; Noda et al., 2008; Mazarico et al., 2011; Speyerer and Robinson, 2013), and, also as on Mercury, these regions are sufficiently cold to host thermally stable water ice (Paige et al., 2010). However, in contrast to Mercury, Earth-based radar observations of the Moon do not show extensive radar-bright deposits in these shadowed regions (Stacy et al., 1997; B. A. Campbell et al., 2003; D. B. Campbell et al., 2006). Spacecraft radar observations, although suggestive of the potential for patchy occurrences of lunar ice, have not shown evidence for lunar water ice deposits in quantities comparable to the deposits in the polar regions of Mercury (Nozette et al., 1996; Simpson and Tyler, 1999; Spudis et al., 2010; Neish et al., 2011; Thomson et al., 2012). Neutron spectrometer measurements indicate enhanced hydrogen in the polar regions of the Moon, but the inferred concentrations are substantially lower than those observed at Mercury (Feldman et al., 1998, 2000, 2001; Lawrence et al., 2006; Teodoro et al., 2010; Mitrofanov et al., 2010; Basilevsky et al., 2012; Miller et al., 2012). Similarly, water vapor detected in the ejecta plume from the Lunar Crater Observation and Sensing Satellite (LCROSS) suggested $5.6 \pm 2.9\%$ by mass for water ice in the lunar regolith at the permanently shadowed impact site within Cabeus crater (Colaprete et al., 2010), a weight fraction considerably lower than Mercury's relatively pure water ice deposits. While it is possible that higher concentrations of water ice are buried in the lunar subsurface, as a result of the downward migration of water ice from impact gardening, temperature oscillations, or changing thermal environments during the Moon's orbital evolution (Schorghofer and Taylor, 2007; Siegler et al., 2011, 2015, 2016), similar measurements conducted at both bodies indicate that Mercury's polar regions contain substantially more water ice than the polar regions on the Moon.

Furthermore, whereas laser reflectance measurements at 1064 nm for Mercury have revealed both low-reflectance and high-reflectance surfaces for the polar deposits, similar observations at the Moon have shown permanently shadowed surfaces with reflectance values only ~10% higher than average, indicative of modest amounts of water frost or a reduction in the effectiveness of space weathering (Lucey et al., 2014). No permanently shadowed regions with low-reflectance surfaces at 1064 nm have been seen on the Moon. Visible-wavelength

imaging of permanently shadowed lunar craters has not revealed surfaces with anomalously high- or low-reflectance surfaces (Haruyama et al., 2008; Speyerer and Robinson, 2013), such as those seen in comparable images of Mercury's polar deposits. Observations at far-ultraviolet wavelengths of permanently shadowed lunar craters indicate redder, low-reflectance surfaces, consistent with high porosity and ~1–2 wt% water frost (Gladstone et al., 2012).

Although the Moon presently shows evidence for water ice in its polar regions, the form of the deposits is qualitatively different from that of polar deposits on Mercury (Lawrence, 2017). Thus, there is a fundamental difference between the volatile inventories of Mercury and the Moon, and resolving this enigma is central to advancing our understanding of the evolution of volatiles across the inner solar system.

13.3.2.2 Implications for the Source

The proposed sources for Mercury's water ice can be divided into four major categories: interactions with the solar wind, outgassing from Mercury's interior, delivery by micrometeoroids, or delivery by one or more large impact events. Table 13.1 summarizes some implications of the observational constraints discussed in the previous section for each of these proposed sources. It is possible, of course, that a combination of processes has acted together to deliver water to Mercury's polar regions, and it is also possible that different processes have provided the dominant source of water ice on Mercury and the Moon.

Solar wind interactions that could create water molecules are expected on both Mercury and the Moon, and Mercury's

proximity to the Sun and the stronger interplanetary magnetic field could result in differences between the two bodies. However, solar wind interactions face other difficulties as the dominant source of Mercury's polar deposits. In particular, the production of other volatile materials to create the low-reflectance deposits observed on Mercury is not predicted. Additionally, an ongoing and steady production of water molecules by solar wind interactions, and their migration to the polar cold traps, has not been shown to be consistent with the extensive and relatively pure nature of Mercury's polar water ice deposits.

Mercury and the Moon have different surface chemical compositions and volcanic histories. Different histories of planetary outgassing could therefore be envisioned for the two bodies, potentially providing different amounts of water and other volatiles available to be cold-trapped in the polar regions. From MESSENGER, we now know that Mercury is more enhanced in volatiles than previously expected (Chapter 2), that volcanism, including pyroclastic eruptions that released magmatic volatiles, was a widespread process in shaping the planet (Chapter 11), and that some volatile loss may indeed still be occurring on Mercury at present, as evidenced by hollows (Chapter 12). The sharp boundaries and distinct surface reflectance of the polar deposits would require planetary outgassing within Mercury's recent past to maintain these characteristics. The rate of accumulation of water ice in Mercury's polar cold traps from outgassing would have to be considerably higher than that of regolith gardening and other surface modification processes to produce the high purity of water ice in Mercury's polar deposits. Whereas Mercury's surface composition is now

Table 13.1. *Implications for possible sources of Mercury's water ice from observational constraints of the planet's polar deposits.*

Source	Constraints on Mercury's polar water ice deposits			
	Not solely water ice	Distinct surface reflectances with sharp boundaries	Relatively pure water ice	Not seen on the Moon
Solar wind interactions	Not predicted	Ongoing process may maintain reflectances, but low-reflectance surfaces are not predicted	Regular and steady process not expected to produce pure deposits	Solar wind interactions occur on both but may manifest differently on Mercury and the Moon
Planetary outgassing	Low-reflectance deposits are volatiles from volcanic eruptions	Would need to be active at present or in recent past to explain surface reflectances	Rate of accumulation from outgassing would have to be faster than regolith mixing	Different compositions and volcanic histories can result in different outgassing
Micrometeoroids	Low-reflectance deposits are organic compounds and volatiles from micrometeoroids	Ongoing process may maintain surface reflectances and sharp boundaries	Regular and steady process not expected to produce pure deposits	Flux of micrometeoroids on Mercury is much larger than on the Moon
Large impact events	Low-reflectance deposits are organic compounds and volatiles from comets or asteroids	Occurred geologically recently to account for the sharp boundaries and surface reflectances	Episodic process can produce pure deposits by emplacement of large volumes of ice at one time	Mercury experienced a recent large impact event; the Moon has not but may have in the past

known to include volatiles, measurements of surface elemental abundances indicate that the planet's chemical composition is highly reduced (Chapter 2). An examination of the nature of possible magmatic volatiles that are expected given Mercury's chemically reduced conditions suggests that its interior is depleted in H and H₂O, and that a combination of C-, S-, Cl-, and Ni-bearing gases drove its pyroclastic activity (Zolotov, 2011). If interior is depleted in water, planetary outgassing would not be likely to produce the broad distribution and dominantly water ice composition of polar deposits that are observed.

Differences between the populations of regularly impacting micrometeoroids could also deliver different amounts of water to Mercury and the Moon, accounting for the different volatile inventories in the polar regions of the two bodies. With an analytical approach, Cintala (1992) calculated that the micrometeoroid flux is 5.5 times greater at Mercury than at the Moon. More recently, with a numerical approach, Borin et al. (2009, 2016) concluded that substantially more micrometeoroids impact Mercury than the Moon, with a flux that is ~58 times higher than that reported by Cintala (1992). Borin et al. (2009, 2016) assumed that the source of micrometeoroids was the main asteroid belt, whereas dynamical modeling work by Nesvorný et al. (2010) suggests that >90% of inner solar system micrometeoroids arise from Jupiter-family comets. This different source for the micrometeoroids would require the numerically modeled impact rate at Mercury to be scaled (Borin et al., 2009); one estimate gives the flux at Mercury as ~39 times greater than that at the Moon (Bruck Syal et al., 2015). However, cometary particles would also each contain greater amounts of water for delivery to Mercury. Monte Carlo models indicate that 20–50% of water molecules emplaced anywhere on the lunar surface will migrate to lunar cold traps, whereas Mercury's cold traps would capture 5–15% of such molecules (Butler, 1997). From simulations that account for the impacting populations, impact velocity, impact angle, and material properties, Bruck Syal and Schultz (2015) concluded that micrometeoroids provide >99% of Mercury's delivered water whereas water delivery to the Moon is dominated at >95% by asteroids. However, although a steady and ongoing process such as micrometeoroid bombardment can be envisioned to regularly refresh the surfaces of Mercury's polar deposits, perhaps creating the distinctive reflectances and sharp boundaries observed, it may be challenging for this process to build up extensive water ice deposits that have the purity determined on Mercury. Thus, while there is general agreement that substantially more micrometeoroids impact Mercury than the Moon, quantitatively robust models are needed to understand the delivery of water to Mercury by micrometeoroids, the subsequent evolution of that water, and the rate of its accumulation in polar cold traps relative to other processes, as well as to investigate whether micrometeoroids are a dominant source for the delivery of water to either object.

Alternatively, an episodic source, such as the impact of one or several large comets or volatile-rich asteroids, could yield the differences in the water ice concentrations observed in the polar regions of Mercury and the Moon. Monte Carlo simulations by Moses et al. (1999) indicated that a small number of massive objects might have delivered most of Mercury's water

inventory, with Jupiter-family comets in particular having the potential to deliver large amounts of water to the planet. If a small number of large impacts were the dominant source for water ice on Mercury or the Moon, then differences between the inventories of these two bodies would be expected, depending on how long the most recent such impact occurred on each object. In such a scenario, Mercury's presently extensive water ice deposits could indicate that a large impact delivered water to the planet in the relatively recent past, whereas the Moon may have experienced such events in the more distant past, perhaps as much as billions of years ago (Siegler et al., 2015, 2016). The differences in characteristics of water ice deposits among different lunar polar cold traps has been suggested as evidence for an episodic rather than steady-state source (Spudis et al., 2010; Miller et al., 2014). A relatively recent event, such as the impact of a large comet or asteroid in the recent past, provides a natural explanation for Mercury's relatively pure water ice deposits with their sharp boundaries and their distinctive surface reflectances arising from low-reflectance, organic-rich volatile compounds delivered by the impactor at the same time as the water ice.

A major question for a large comet or asteroid impact source is whether the water ice can survive the energetic impact event. Modeling the volatile retention from cometary impacts on the Moon, Ong et al. (2010) found that impacts at low velocities (~5 km/s) retain nearly all of the water but at high velocities (~60 km/s) nearly all of the water is lost. Overall, Ong et al. (2010) concluded that asteroids provide six times more water to the Moon than comets and that such delivery could match the measured lunar concentrations of water ice. However, impacts on Mercury have a higher average impact velocity and span a larger overall range of impact velocities (Le Feuvre and Wieczorek, 2008; Marchi et al., 2009), which could decrease water retention during the impact event, though the larger surface gravitational acceleration could increase retention relative to the Moon. On the basis of a comet-impact simulation on the Moon that began with the impact event and followed the water until it was lost or deposited in a lunar cold trap, Stewart et al. (2011) concluded that ~0.1% of the cometary water was retained on the Moon in polar cold traps. They also concluded that migration of water molecules by hopping on the lunar surface, such as modeled by Butler (1997), is not the most important process for the transport and deposition that occurs during a large impact, given the density of the initial gas in the comet impact and the potential for the creation of a transient atmosphere (Stewart et al., 2011). Impact simulations at 45°N and 45°S latitudes predicted trapping of water molecules near both the lunar north and south poles (Stewart et al., 2011), suggesting that a large impact event could be responsible for water ice being transported to both polar regions. Subsequent numerical simulations indicated that a transient, impact-generated lunar atmosphere could be sufficiently dense that its lower layers are shielded from photodestruction, prolonging the lifetime of water molecules and allowing greater amounts of water to reach lunar polar cold traps (Prem et al., 2015). Similar modeling of a large impact event on Mercury would provide valuable insight into the possibility that Mercury's water ice was delivered by a large impact, especially considering the differences in the gravitational

acceleration, impact velocity, rotation rate, and thermal environment between the Moon and Mercury.

Given that Mercury's total water ice abundance is estimated at $\sim 10^{16}$ – 10^{18} g (Moses et al., 1999; Lawrence et al., 2013) and that estimates for the amount of impacting water captured in polar cold traps range from $\sim 0.1\%$ (for a cometary impact on the Moon rather than Mercury) (Stewart et al., 2011) to $\sim 1\%$ (for Monte Carlo modeling of Jupiter-family comets impacting Mercury followed by random-hop migration) (Butler, 1997; Moses et al., 1999), a single impacting object would have to contain 10^{18} – 10^{21} g of water. Given that a comet of pure water ice without porosity provides a lower limit to the size of such an impacting object, an impactor diameter of at least ~ 10 – 100 km would be needed. The diameter of the crater associated with such an impact would be approximately an order of magnitude larger than that of the impacting object and would depend on impact conditions (e.g., Collins et al., 2005). There are considerable uncertainties associated with this simple estimate, but if a single impact event delivered all of the water ice observed in Mercury's polar deposits, such an impact should have produced a sizable crater. The 96-km-diameter crater Hokusai is distinctive, as it is one of Mercury's youngest large craters and its formation generated the planet's longest set of rays, which extend for thousands of kilometers (Xiao et al., 2016). The size of Hokusai crater is on the lower end of estimates for the source crater of Mercury's water ice deposits (Ernst et al., 2016), but size alone is insufficient to rule out Hokusai as a source-crater candidate because of the uncertainties currently associated with estimates for the retention of volatiles on Mercury during impact events. In general, if the sources of Mercury's water ice deposits were large, recent impact events, investigations to identify the corresponding crater or craters should be pursued.

In summary, a recent large impact event can most easily account for the observed constraints on Mercury's polar deposits, but there is much work left to be done to examine the proposed source hypotheses further, given the new results from the MESSENGER mission.

13.4 FUTURE EXPLORATION

Results from the MESSENGER mission, combined with previous Earth-based radar observations, provide multiple lines of evidence that Mercury's polar deposits are composed of substantial amounts of water ice. Moreover, the characteristics of the water ice deposits, such as the presence of low-reflectance volatiles, the distinctive surface reflectances, the relative purity of the water ice, and the contrast with the polar regions on the Moon, provide constraints on the source of the water, and hence on its age and evolution. Future research can provide important insights into the origin and evolution of water ice on Mercury and the delivery of volatiles throughout the inner solar system.

Further analyses of MESSENGER data are needed. These include, but are not limited to, high-resolution studies to explore specific water-ice-bearing craters, analyses to constrain the depth and thickness of the water ice deposits,

investigations of small craters that host water ice deposits, and models of the reflectance properties of the deposits in relation to their purity and surface composition. The MESSENGER results also provide a clear rationale for modeling efforts to simulate the wide-ranging processes that have been hypothesized as the source of Mercury's water ice. Additional Earth-based radar observations could provide insight into the similarities and differences between individual deposits and improve overall coverage, especially in the south polar region.

BepiColombo, a joint mission of the European Space Agency and the Japan Aerospace Exploration Agency (Benkhoff et al., 2010), which is currently scheduled to launch in 2018 and to insert two spacecraft into orbit about Mercury in 2025, has the opportunity to provide new observations of Mercury's water ice deposits (Chapter 20). The majority of MESSENGER's observations of Mercury's polar deposits were limited to the north polar region because of the spacecraft's highly eccentric orbit and high northern periapsis, whereas BepiColombo's Mercury Planetary Orbiter (MPO) will have a near-equatorial periapsis and should pass at similar altitudes over both of Mercury's poles. Depending on the final altitude of MPO, BepiColombo could provide the first neutron spectrometry, laser altimetry, and visible-wavelength imaging of the shadowed surfaces of the water ice deposits in Mercury's south polar region. Such measurements would be complementary to similar measurements made by MESSENGER for the north polar region. Additionally, the Mercury Radiometer and Thermal Infrared Spectrometer (MERTIS) instrument on BepiColombo's MPO includes an infrared spectrometer that will operate in the wavelength range 7–14 μm and a radiometer that will operate in the wavelength range 7–40 μm , and there are plans to operate in a special "polar mode" to enable measurements of Mercury's polar deposits (Hiesinger et al., 2010). No such measurements were made by MESSENGER, so MERTIS has the potential to provide new compositional and thermal measurements of Mercury's polar deposits. In particular, MERTIS spectral measurements may constrain the composition of the low-reflectance layer that covers the majority of Mercury's polar deposits. Such information could test hypotheses for the source of Mercury's water ice and would have implications for the distribution of volatiles in the solar system.

Future exploration of Mercury by spacecraft after BepiColombo that are focused on understanding Mercury's water ice deposits or the inventory of inner solar system volatiles may use landed payloads, providing sensitive chemical and isotopic measurements not possible from remote orbital observations. Resolving the differences between Mercury's extensive water ice deposits and the polar volatile deposits measured on the Moon remains a fundamental question tied to the overarching goal to understand the sources and evolution of water in the inner solar system. In situ measurements of water on both the Moon and Mercury will be key to resolving these questions and gaining this larger understanding, including an understanding of the sources of water on Earth.

REFERENCES

- Barnouin, O. S., Zuber, M. T., Smith, D. E., Neumann, G. A., Herrick, R. R., Chappelow, J. E., Murchie, S. L. and Prockter, L. M. (2012). The morphology of craters on Mercury: Results from MESSENGER flybys. *Icarus*, **219**, 414–427.
- Basilevsky, A. T., Abdrakhimov, A. M. and Dorofeeva, V. A. (2012). Water and other volatiles on the Moon: A review. *Solar Syst. Res.*, **46**, 89–107.
- Benkhoff, J., van Casteren, J., Hayakawa, H., Fujimoto, M., Laakso, H., Novara, M., Ferri, P., Middleton, H. R. and Ziethe, R. (2010). BepiColombo – Comprehensive exploration of Mercury: Mission overview and science goals. *Planet. Space Sci.*, **58**, 2–20.
- Black, G. J., Campbell, D. B. and Nicholson, P. D. (2001). Icy Galilean satellites: Modeling radar reflectivities as coherent backscatter effect. *Icarus*, **151**, 167–180.
- Black, G. J., Campbell, D. B. and Harmon, J. K. (2010). Radar measurements of Mercury's north pole at 70 cm wavelength. *Icarus*, **209**, 224–229, doi:10.1016/j.icarus.2009.10.009.
- Borin, P., Cremonese, G., Marzari, F., Bruno, M. and Marchi, S. (2009). Statistical analysis of micrometeoroids flux on Mercury. *Astron. Astrophys.*, **503**, 259–264, doi:10.1051/0004-6361/200912080.
- Borin, P., Cremonese, G., Bruno, M. and Marzari F. (2016). Asymmetries in the dust flux at Mercury. *Icarus*, **264**, 220–226.
- Botta, O. and Bada, J. L. (2002). Extraterrestrial organic compounds in meteorites. *Surv. Geophys.*, **23**, 411–467.
- Bruck Syal, M. and Schultz, P. H. (2015). Impact delivery of water at the Moon and Mercury. *Lunar Planet. Sci.*, **46**, abstract 1680.
- Bruck Syal, M., Schultz, P. H. and Riner, M. A. (2015). Darkening of Mercury's surface by cometary carbon. *Nature Geosci.*, **8**, 352–356, doi:10.1038/NGE02397.
- Bussey, D. B. J., Spudis, P. D. and Robinson, M. S. (1999). Illumination conditions at the lunar south pole. *Geophys. Res. Lett.*, **26**, 1187–1190.
- Bussey, D. B. J., Fristad, K. E., Schenk, P. M., Robinson, M. S. and Spudis, P. D. (2005). Constant illumination at the lunar north pole. *Nature*, **434**, 842.
- Bussey, D. B. J., McGovern, J. A., Spudis, P. D., Neish, C. D., Noda, H., Ishihara, Y. and Sorensen, S.-A. (2010). Illumination conditions of the south pole of the Moon derived using Kaguya topography. *Icarus*, **208**, 558–564.
- Butler, B. J. (1997). The migration of volatiles on the surfaces of Mercury and the Moon. *J. Geophys. Res.*, **102**, 19,283–19,291.
- Butler, B. J., Muhleman, D. O. and Slade, M. A. (1993). Mercury: Full-disk radar images and the detection and stability of ice at the north pole. *J. Geophys. Res.*, **98**, 15,003–15,023.
- Campbell, B. A., Campbell, D. B., Chandler, J. F., Hine, A. A., Nolan, M. C. and Perillat, P. J. (2003). Radar imaging of the lunar poles. *Nature*, **426**, 137–148.
- Campbell, D. B., Chandler, J. F., Ostro, S. J., Pettengill, G. H. and Shapiro, I. I. (1978). Galilean satellites: 1976 radar results. *Icarus*, **34**, 254–267.
- Campbell, D. B., Campbell, B. A., Carter, L. M., Margot, J.-L. and Stacy, N. J. S. (2006). No evidence for thick deposits of ice at the lunar south pole. *Nature*, **443**, 835–837.
- Carrier, W. D., III, Olhoef, G. R. and Mendell W. (1991). Physical properties of the lunar surface. In *Lunar Sourcebook: A User's Guide to the Moon*, ed. G. Heiken, D. Vaniman and B. M. French. Cambridge: Cambridge University Press, pp. 475–594.
- Cavanaugh, J. F., Smith, J. C., Sun, X., Bartels, A. E., Ramos-Izquierdo, L., Krebs, D. J., McGarry, J. F., Trunzo, R., Novo-Gradac, A. M., Britt, J. L., Karsh, J., Katz, R. B., Lukemire, A. T., Szymkiewicz, R., Berry, D. L., Swinski, J. P., Neumann, G. A., Zuber, M. T. and Smith, D. E. (2007). The Mercury Laser Altimeter instrument for the MESSENGER mission. *Space Sci. Rev.*, **131**, 451–480.
- Chabot, N. L., Ernst, C. M., Denevi, B. W., Harmon, J. K., Murchie, S. L., Blewett, D. T., Solomon, S. C. and Zhong, E. D. (2012). Areas of permanent shadow in Mercury's south polar region ascertained by MESSENGER orbital imaging. *Geophys. Res. Lett.*, **39**, L09204, doi:10.1029/2012GL051526.
- Chabot, N. L., Ernst, C. M., Harmon, J. K., Murchie, S. L., Solomon, S. C., Blewett, D. T. and Denevi, B. W. (2013). Craters hosting radar-bright deposits in Mercury's north polar region: Areas of persistent shadow determined from MESSENGER images. *J. Geophys. Res. Planets*, **118**, 26–36.
- Chabot, N. L., Ernst, C. M., Denevi, B. W., Nair, H., Deutsch, A. N., Blewett, D. T., Murchie, S. L., Neumann, G. A., Mazarico, E., Paige, D. A., Harmon, J. K., Head, J. W. and Solomon, S. C. (2014). Images of surface volatiles in Mercury's polar craters acquired by the MESSENGER spacecraft. *Geology*, **42**, 1051–1054.
- Chabot, N. L., Ernst, C. M., Paige, D. A., Nair H., Denevi, B. W., Blewett, D. T., Murchie, S. L., Deutsch, A. N., Head, J. W. and Solomon, S. C. (2016). Imaging Mercury's polar deposits during MESSENGER's low-altitude campaign. *Geophys. Res. Lett.*, **43**, 9461–9468.
- Cintala, M. J. (1992). Impact-induced thermal effects in the lunar and mercurian regoliths. *J. Geophys. Res.*, **97**, 947–973.
- Colaprete, A., Schultz, P., Heldmann, J., Wooden, D., Shirley, M., Ennico, K., Hermaly, B., Marshall, W., Ricco, A., Elphic, R. C., Goldstein, D., Summy, D., Bart, G. D., Asphaug, E., Korycansky, D., Landis, D. and Sollitt, L. (2010). Detection of water in the LCROSS ejecta plume. *Science*, **330**, 463–468.
- Collins, G. S., Melosh, H. J. and Marcus, R. A. (2005). Earth impact effects program: A web-based computer program for calculating the regional environmental consequences of a meteoroid impact on Earth. *Meteorit. Planet. Sci.*, **40**, 817–840.
- Crider, D. and Killen, R. M. (2005). Burial rate of Mercury's polar volatile deposits. *Geophys. Res. Lett.*, **32**, L12201, doi:10.1029/2005GL022689.
- Crites, S. T., Lucey, P. G. and Lawrence, D. J. (2013). Proton flux and radiation dose from galactic cosmic rays in the lunar regolith and implications for organic synthesis at the poles of the Moon and Mercury. *Icarus*, **226**, 1192–1200.
- Davies, M. E., Dwornik, S. E., Gault, D. E. and Strom, R. G. (1978). *Atlas of Mercury*, Special Publication SP-423. Washington, DC: National Aeronautics and Space Administration.
- Delitsky, M. L., Paige, D. A., Siegler, M. A., Harju, E. R., Schriver, D., Johnson, R. E. and Travnicek, P. (2017). Ices on Mercury: Chemistry of volatiles in permanently cold areas of Mercury's north polar region. *Icarus*, **281**, 19–31.
- Deutsch, A. N., Chabot, N. L., Mazarico, E., Ernst, C. M., Head, J. W., Neumann, G. A. and Solomon, S. C. (2016). Comparison of areas in shadow in the north polar region of Mercury from imaging and altimetry, with implications for polar ice deposits. *Icarus*, **280**, 158–171.
- Deutsch, A. N., Neumann, G. A. and Head, J. W. (2017a). New evidence for surface water ice in small-scale cold traps and in three large craters at the north polar region of Mercury from the Mercury Laser Altimeter. *Geophys. Res. Lett.*, **44**, 9233–9241, doi:10.1002/2017GL074723.
- Deutsch, A. N., Head, J. W., Neumann, G. A. and Chabot, N. L. (2017b). Constraining the depth of polar ice deposits and evolution of cold traps on Mercury with small craters in permanently shadowed regions. *Lunar Planet. Sci.*, **48**, abstract 1634.
- Eke, V. R., Lawrence, D. J. and Teodoro, L. F. A. (2017). How thick are Mercury's polar water deposits? *Icarus*, **284**, 407–415.
- Ernst, C. M., Chabot, N. L., Susorney, H. C., Barnouin, O. S., Harmon, J. K. and Paige, D. A. (2014). Exploring the morphology of simple

- craters that host polar deposits on Mercury: Implications for the source and stability of water ice. *Lunar Planet. Sci.*, **45**, abstract 1238.
- Ernst, C. M., Chabot, N. L. and Barnouin, O. S. (2016). Examining the potential contributions of the Hokusai impact to water ice on Mercury. *Lunar Planet. Sci.*, **47**, abstract 1374.
- Feldman, W. C. and Drake, D. M. (1986). A Doppler filter technique to measure the hydrogen content of planetary surfaces. *Nucl. Instrum. Methods A*, **245**, 182–190.
- Feldman, W. C., Drake, D. M., O'Dell, R. D., Brinkley, F. W., Jr. and Anderson, R. C. (1989). Gravitational effects on planetary neutron flux spectra. *J. Geophys. Res.*, **94**, 513–525.
- Feldman, W. C., Barraclough, B. L., Hansen, C. J. and Sprague, A. L. (1997). The neutron signature of Mercury's volatile polar deposits. *J. Geophys. Res.*, **102**, 25,565–25,574.
- Feldman, W. C., Maurice, S., Binder, A. B., Barraclough, B. L., Elphic, R. C. and Lawrence, D. J. (1998). Fluxes of fast and epithermal neutrons from Lunar Prospector: Evidence for water ice at the lunar poles. *Science*, **281**, 1496–500.
- Feldman, W. C., Lawrence, D. J., Elphic, R. C., Barraclough, B. L., Maurice, S., Genetay, I. and Binder, A. B. (2000). Polar hydrogen deposits on the Moon. *J. Geophys. Res.*, **105**, 4175–4195.
- Feldman, W. C., Maurice, D., Lawrence, D. J., Little, R. C., Lawson, S. L., Gasnault, O., Wiens, R. C., Barraclough, B. L., Elphic, R. C., Prettyman, T. H., Steinberg, J. T. and Binder, A. B. (2001). Evidence for water ice near the lunar poles. *J. Geophys. Res.*, **106**, 23,231–23,251, doi:10.1029/2000JE001444.
- Feldman, W. C., Boynton, W. V., Tokar, R. L., Prettyman, T. H., Gasnault, O., Squyres, S. W., Elphic, R. C., Lawrence, D. J., Lawson, S. L., Maurice, S., McKinnet, G. W., Moore, K. R. and Reedy, R. C. (2002). Global distribution of neutrons from Mars: Results from Mars Odyssey. *Science*, **297**, 75–78.
- Feldman, W. C., Mellon, M. T., Gasnault, O., Diez, B., Elphic, R. C., Hagerty, J. J., Lawrence, D. J., Maurice, S. and Prettyman, T. H. (2007). Vertical distribution of hydrogen at high northern latitudes on Mars: The Mars Odyssey Neutron Spectrometer. *Geophys. Res. Lett.*, **34**, L05201, doi:10.1029/2006GL028530.
- Gladstone, G. R., Retherford, K. D., Egan, A. F., Kaufmann, D. E., Miles, P. F., Parker, J. W., Horvath, D., Rojas, P. M., Versteeg, M. H., Davis, M. W., Greathouse, T. K., Slater, D. C., Mukherjee, J., Steffl, A. J., Feldman, P. D., Hurley, D. M., Pryor, W. R., Hendrix, A. R., Mazarico, E. and Stern, S. A. (2012). Far-ultraviolet reflectance properties of the Moon's permanently shadowed regions. *J. Geophys. Res.*, **117**, E00H04, doi:10.1029/2011JE003913.
- Goldsten, J. O., Rhodes, E. A., Boynton, W. V., Feldman, W. C., Lawrence, D. J., Trombka, J. I., Smith, D. M., Evans, L. G., White, J., Madden, N. W., Berg, P. C., Murphy, G. A., Gurnee, R. S., Strohbehn, K., Williams, B. D., Schaefer, E. D., Monaco, C. A., Cork, C. P., Del Eckels, J., Miller, W. O., Burks, M. T., Hagler, L. B., DeTeresa, S. J. and Witte, M. C. (2007). The MESSENGER Gamma-Ray and Neutron Spectrometer. *Space Sci. Rev.*, **131**, 339–391.
- Hapke, B. (1990). Coherent backscatter and the radar characteristics of outer planet satellites. *Icarus*, **88**, 407–17.
- Hapke, B. and Blewett, D. (1991). Coherent backscatter model for the unusual radar reflectivity of icy satellites. *Nature*, **352**, 46–47.
- Harcke, L. J. (2005). Radar imaging of solar system ices. Ph.D. thesis, Stanford University, Stanford, CA, 201 pp.
- Harmon, J. K. (2007). Radar imaging of Mercury. *Space Sci. Rev.*, **132**, 307–349.
- Harmon, J. K. and Slade, M. A. (1992). Radar mapping of Mercury: Full-disk images and polar anomalies. *Science*, **258**, 640–643.
- Harmon, J. K., Perillat, P. J. and Slade, M. A. (2001). High-resolution radar imaging of Mercury's north pole. *Icarus*, **149**, 1–15.
- Harmon, J. K., Slade, M. A., Vélez, R. A., Crespo, A., Dryer, M. J. and Johnson, J. M. (1994). Radar mapping of Mercury's polar anomalies. *Nature*, **369**, 213–215.
- Harmon, J. K., Slade, M. A. and Rice, M. S. (2011). Radar imagery of Mercury's putative polar ice: 1999–2005 Arecibo results. *Icarus*, **211**, 37–50.
- Haruyama, J., Ohtake, M., Matsunaga, T., Morota, T., Honda, C., Yokota, Y., Pieters, C. M., Hara, S., Hioki, K., Saiki, K., Miyamoto, H., Iwasaki, A., Abe, M., Ogawa, Y., Takeda, H., Shirao, M., Yamaji, A. and Josset, J. L. (2008). Lack of exposed ice inside lunar south pole Shackleton crater. *Science*, **322**, 938–939, doi:10.1126/science.1164020.
- Hawkins, S. E., III, Boldt, J. D., Darlington, E. H., Espiritu, R., Gold, R. E., Gotwols, B., Grey, M. P., Hash, C. D., Hayes, J. R., Jaskulek, S. E., Kardian, C. J., Jr., Keller, M. R., Malaret, E. R., Murchie, S. L., Murphy, P. K., Peacock, K., Prockter, L. M., Reiter, R. A., Robinson, M. S., Schaefer, E. D., Shelton, R. G., Sterner, R. E., II, Taylor, H. W., Watters, T. R. and Williams, B. D. (2007). The Mercury Dual Imaging System on the MESSENGER spacecraft. *Space Sci. Rev.*, **131**, 247–338.
- Hiesinger, H., Helbert, J. and MERTIS Co-I Team (2010). The Mercury Radiometer and Thermal Infrared Spectrometer (MERTIS) for the BepiColombo mission. *Planet. Space Sci.*, **58**, 144–165.
- Ingersoll, A. P., Svitek, T. and Murray, B. C. (1992). Stability of polar frosts in spherical bowl-shaped craters on Moon, Mercury, and Mars. *Icarus*, **100**, 40–47.
- Lawrence, D. J. (2017). A tale of two poles: Toward understanding the presence, distribution, and origin of volatiles at the polar regions of the Moon and Mercury. *J. Geophys. Res. Planets*, **122**, 21–52.
- Lawrence, D. J., Feldman, W. C., Elphic, R. C., Hagerty, J. J., Maurice, S., McKinnety, G. W. and Prettyman, T. H. (2006). Improved modeling of Lunar Prospector neutron spectrometer data: Implications for hydrogen deposits at the lunar poles. *J. Geophys. Res.*, **111**, E08001, doi:10.1029/2005JE002637.
- Lawrence, D. J., Harmon, J. K., Feldman, W. C., Goldsten, J. O., Paige, D. A., Peplowski, P. N., Rhodes, E. A., Selby, C. M. and Solomon S. C. (2011). Predictions of MESSENGER Neutron Spectrometer measurements of Mercury's north polar region. *Planet. Space Sci.*, **59**, 1665–1669.
- Lawrence, D. J., Feldman, W. C., Goldsten, J. O., Maurice, S., Peplowski, P. N., Anderson, B. J., Bazell, D., McNutt, R. L., Nittler, L. R., Prettyman, T. H., Rodgers, D. J., Solomon, S. C. and Weider, S. Z. (2013). Evidence for water ice near Mercury's north pole from MESSENGER Neutron Spectrometer measurements. *Science*, **339**, 292–296, doi:10.1126/science.1229953.
- Le Feuvre, M. and Wieczorek, M. A. (2008). Nonuniform cratering of the terrestrial planets. *Icarus*, **197**, 291–306.
- Li, L. and Mustard, J. F. (2000). Compositional gradients across mare-highland contacts: Importance and geological implication of lateral transport. *J. Geophys. Res.*, **105**, 20,431–20,450.
- Lucey, P. G., Neumann, G. A., Riner, M. A., Mazarico, E., Smith, D. E., Zuber, M. T., Paige, D. A., Bussey, D. B., Cahill, J. T., McGovern, A., Isaacson, P., Corley, L. M., Torrence, M. H., Melosh, H. J., Head, J. W. and Song, E. (2014). The global albedo of the Moon at 1064 nm from LOLA. *J. Geophys. Res. Planets*, **119**, 1665–1679, doi:10.1002/2013JE004592.
- Marchi, S., Mottola, S., Cremonese, G., Massironi, M. and Martellato, E. (2009). A new chronology for the Moon and Mercury. *Astron. J.*, **137**, 4936–4948.
- Margot, J.-L., Peale, S. J., Solomon, S. C., Hauck, S. A., II, Ghigo, F. D., Jurgens, R. F., Yseboodt, M., Giorgini, J. D., Padovan, S. and Campbell, D. B. (2012). Mercury's moment of inertia from spin and gravity data. *J. Geophys. Res.*, **117**, E00L09, doi:10.1029/2012JE004161.

- Mazarico, E., Neumann, G. A., Smith, D. E., Zuber, M. T. and Torrence, M. H. (2011). Illuminations conditions of the lunar polar regions using LOLA topography. *Icarus*, **211**, 1066–1081.
- Mazarico, E., Nicholas, J. B., Neumann, G. A., Smith, D. E. and Zuber, M. T. (2014). Illumination conditions at the poles of the Moon and Mercury, and application to data analysis. *Lunar Planet. Sci.*, **45**, abstract 1867.
- McCord, T. B., Taylor, L. A., Combe, J.-P., Kramer, G., Pieters, C. M., Sunshine, J. M. and Clark, R. N. (2011). Sources and physical processes responsible for OH/H₂O in the lunar soil as revealed by the Moon Mineralogy Mapper (M³). *J. Geophys. Res.*, **116**, E00G05, doi:10.1029/2010JE003711.
- Miller, R. S., Nerurkar, G. and Lawrence, D. J. (2012). Enhanced hydrogen at the lunar poles: New insights from the detection of epithermal and fast neutron signatures. *J. Geophys. Res.*, **117**, E11007, doi:10.1029/2012JE004112.
- Miller, R. S., Lawrence, D. J. and Hurley, D. M. (2014). Identification of surface hydrogen enhancements within the Moon's Shackleton crater. *Icarus*, **233**, 229–232.
- Mitrofanov, I. G., Sanin, A. B., Boynton, W. V., Chin, G., Garvin, J. B., Golovin, D., Evans, L. G., Harshman, K., Kozyrev, A. S., Litvak, M. L., Malakhov, A., Mazarico, E., McClanahan, T., Milikh, G., Mokrousov, M., Nandikotkur, G., Neumann, G. A., Nuzhdin, I., Sagdeev, R., Shevchenko, V., Shvetsov, V., Smith, D. E., Starr, R., Tret'yakov, V. I., Trombka, J., Usikov, D., Varenikov, A., Vostrukhin, A. and Zuber, M. T. (2010). Hydrogen mapping of the lunar south pole using the LRO neutron detector experiment LEND. *Science*, **330**, 483–486.
- Morgan, T. H. and Shemansky, D. C. (1991). Limits to the lunar atmosphere. *J. Geophys. Res.*, **96**, 1351–1367.
- Moses, J. I., Rawlins, K., Zahnle, K. and Dones, L. (1999). External sources of water for Mercury's putative ice deposits. *Icarus*, **137**, 197–221.
- Muhleman, D. O., Butler, B. J., Grossman, A. W. and Slade, M. A. (1991). Radar images of Mars. *Science*, **253**, 1508–1513.
- Neish, C. D., Bussey, D. B. J., Spudis, P., Marshall, W., Thomson, B. J., Patterson, G. W. and Carter, L. M. (2011). The nature of lunar volatiles as revealed by Mini-RF observations of the LCROSS impact site. *J. Geophys. Res.*, **116**, E01005, doi:10.1029/2010JE003647.
- Nesvorný, D., Jenniskens, P., Levison, H. F., Bottke, W. F., Vokrouhlický, D. and Gounelle, M. (2010). Cometary origin of the zodiacal cloud and carbonaceous micrometeorites. Implications for host debris disks. *Astrophys. J.*, **713**, 816–836, doi:10.1088/0004-637X/713/2/816.
- Neumann, G. A., Cavanaugh, J. F., Sun, X., Mazarico, E., Smith, D. E., Zuber, M. T., Mao, D., Paige, D. A., Solomon, S. C., Ernst, C. M. and Barnouin, O. S. (2013). Bright and dark polar deposits on Mercury: Evidence for surface volatiles. *Science*, **339**, 296–300.
- Neumann, G. A., Sun, X., Mazarico, E., Deutsch, A. N., Head, J. W., Paige, D. A., Rubanenko, L. and Susorney, H. C. M. (2017). Latitudinal variation in Mercury's reflectance from the Mercury Laser Altimeter. *Lunar Planet. Sci.*, **48**, abstract 2660.
- Nittler, L. R., Starr, R. D., Weider, S. Z., McCoy, T. J., Boynton, W. V., Ebel, D. S., Ernst, C. M., Evans, L. G., Goldsten, J. O., Hamara, D. K., Lawrence, D. J., McNutt, R. L., Jr., Schlemm, C. E., II, Solomon, S. C. and Sprague, A. L. (2011). The major-element composition of Mercury's surface from MESSENGER X-ray spectrometry. *Science*, **333**, 1847–1850.
- Noda, H., Araki, H., Goossens, S., Ishihara, Y., Matsumoto, K., Tazawa, S., Kawano, N. and Sasaki, S. (2008). Illumination conditions at the lunar polar regions by KAGUYA (SELENE) laser altimeter. *Geophys. Res. Lett.*, **35**, L24203, doi:10.1029/2008GL035692.
- Nozette, S., Lichtenberg, C. L., Spudis, P., Bonner, R., Ort, W., Malaret, E., Robinson, M. and Shoemaker, E. M. (1996). The Clementine bistatic radar experiment. *Science*, **274**, 1495–1498.
- Ong, L., Asphaug, E. I., Korycansky, D. and Coker, R. F. (2010). Volatile retention from cometary impacts on the Moon. *Icarus*, **207**, 578–589.
- Ostro, S. J., Campbell, D. B., Pettengill, G. H. and Shapiro, I. I. (1980). Radar observations of the icy Galilean satellites. *Icarus*, **44**, 431–440.
- Paige, D. A., Wood, S. E. and Vasavada, A. R. (1992). The thermal stability of water ice at the poles of Mercury. *Science*, **258**, 643–646.
- Paige, D. A., Siegler, M. A., Zhang, J. A., Hayne, P. O., Foote, E. J., Bennett, K. A., Vasavada, A. R., Greenhagen, B. T., Schofield, J. T., McCleese, D. J., Foote, M. C., DeJong, E., Bills, B. G., Hartford, W., Murray, B. C., Allen, C. C., Snook, K., Soderblom, L. A., Calcutt, S., Taylor, F. W., Bowles, N. E., Bandfield, J. L., Elphic, R., Ghent, R., Glotch, T. D., Wyatt, M. B. and Lucey, P. G. (2010). Diviner lunar radiometer observations of cold traps in the Moon's south polar region. *Science*, **330**, 479–482.
- Paige, D. A., Siegler, M. A., Harmon, J. K., Neumann, G. A., Mazarico, E. M., Smith, D. E., Zuber, M. T., Harju, E., Delitsky, M. L. and Solomon, S. C. (2013). Thermal stability of volatiles in the north polar region of Mercury. *Science*, **339**, 300–303.
- Paige, D. A., Hayne, D. A., Siegler, M. A., Smith, D. E., Zuber, M. T., Neumann, G. A., Mazarico, E. M., Denevi, B. W. and Solomon, S. C. (2014). Dark surface deposits in the north polar region of Mercury: Evidence for widespread small-scale volatile cold traps. *Lunar Planet. Sci.*, **45**, abstract 2501.
- Peale, S. J. (1988). The rotational dynamics of Mercury and the state of its core. In *Mercury*, ed. F. Vilas, C. R. Chapman and M. S. Matthews. Tucson, AZ: University of Arizona Press, pp. 461–493.
- Pelowitz, D. B. (ed.) (2005). *MCNPX User's Manual, Version 2.5.0*. Report LA-UR-94–1817. Los Alamos, NM: Los Alamos National Laboratory.
- Pierazzo, E. and Chyba, C. F. (1999). Amino acid survival in large cometary impacts. *Meteorit. Planet. Sci.*, **34**, 909–918.
- Pierazzo, E. and Chyba, C. F. (2006). Impact delivery of prebiotic organic matter to planetary surfaces. In *Comets and the Origin and Evolution of Life*, 2nd edn, ed. P. J. Thomas, R. D. Hicks, C. F. Chyba and C. P. McKay. Advances in Astrobiology and Biogeophysics. Berlin: Springer-Verlag, pp. 137–168, doi:10.1007/10903490_5.
- Pike, R. J. (1988). Geomorphology of impact craters on Mercury. In *Mercury*, ed. F. Vilas, C. R. Chapman and M. S. Matthews. Tucson, AZ: University of Arizona Press, pp. 165–273.
- Prem, P., Artemieva, N. A., Goldstein, D. B., Varghese, P. L. and Trafton, L. M. (2015). Transport of water in a transient impact-generated lunar atmosphere. *Icarus*, **255**, 148–158, doi:10.1016/j.icarus.2014.10.017.
- Prettyman, T. H. (2007). Remote chemical sensing using nuclear spectroscopy. In *Encyclopedia of the Solar System*, 2nd edn, ed. L. A. McFadden, P. R. Weissman and T. V. Johnson. San Diego, CA: Academic Press, pp. 765–786.
- Prettyman, T. H., Mittlefehldt, D. W., Yamashita, N., Lawrence, D. J., Beck, A. W., Feldman, W. C., McCoy, T. J., McSween, H. Y., Toplis, M. J., Titus, T. N., Tricarico, P., Reedy, R. C., Hendricks, J. S., Forni, O., Le Corre, L., Li, J.-Y., Mizzon, H., Reddy, V., Raymond, C. A. and Russell, C. T. (2012). Elemental mapping by Dawn reveals exogenic H in Vesta's regolith. *Science*, **338**, 242–246.
- Rubanenko, L., Mazarico, E., Neumann, G. A. and Paige, D. A. (2017). Evidence for surface and subsurface ice inside micro cold-traps on Mercury's north pole. *Lunar Planet. Sci.*, **48**, abstract 1461.
- Salvail, J. R. and Fanale, F. P. (1994). Near-surface ice on Mercury and the Moon: A topographic thermal model. *Icarus*, **111**, 441–455.

- Schorghofer, N. and Taylor, G. J. (2007). Subsurface migration of H₂O at lunar cold traps. *J. Geophys. Res.*, **112**, E02010, doi:10.1029/2006JE002779.
- Siegler, M. A., Bills, B. G. and Paige, D. A. (2011). Effects of orbital evolution on lunar ice stability. *J. Geophys. Res.*, **116**, E03010, doi:10.1029/2010JE003652.
- Siegler, M., Paige, D., Williams, J.-P. and Bills, B. (2015). Evolution of lunar polar ice stability. *Icarus*, **255**, 78–87.
- Siegler, M. A., Miller, R. S., Keane, J. T., Paige, D. A., Matsuyama, I., Lawrence, D. J., Crotts, A. and Poston, M. J. (2016). Lunar true polar wander inferred from polar hydrogen. *Nature*, **531**, 480–484.
- Simpson, R. A. and Tyler, G. L. (1999). Reanalysis of Clementine bistatic radar data from the lunar South Pole. *J. Geophys. Res.*, **104**, 3845–3862.
- Slade, M. A., Butler, B. J. and Muhleman, D. O. (1992). Mercury radar imaging: Evidence for polar ice. *Science*, **258**, 635–640.
- Speyerer, E. J. and Robinson, M. S. (2013). Persistently illuminated regions at the lunar poles: Ideal sites for future exploration. *Icarus*, **222**, 122–136.
- Sprague, A. L., Hunten, D. M. and Lodders, K. (1995). Sulfur at Mercury, elemental at the poles and sulfides in the regolith. *Icarus*, **118**, 211–215.
- Spudis, P. D., Bussey, D. B. J., Baloga, S. M., Butler, B. J., Carl, D., Carter, L. M., Chakraborty, M., Elphic, R. C., Gillis-Davis, J. J., Goswami, J. N., Heggy, E., Hillyard, M., Jensen, R., Kirk, R. L., LaVallee, D., McKerracher, P., Neish, C. D., Nozette, S., Nylund, S., Palsetia, M., Patterson, W., Robinson, M. S., Raney, R. K., Schulze, R. C., Sequeira, H., Skura, J., Thompson, T. W., Thomson, B. J., Ustinov, E. A. and Winters, H. L. (2010). Initial results for the north pole of the Moon from Mini-SAR, Chandrayaan-1 mission. *Geophys. Res. Lett.*, **37**, L06204, doi:10.1029/2009GL042259.
- Stacy, N. J. S., Campbell, D. B. and Ford, P. G. (1997). Arecibo radar mapping of the lunar poles: A search for ice deposits. *Science*, **276**, 1527–1530.
- Starukhina, L. (2001). Water detection on atmosphereless celestial bodies: Alternative explanations of the observations. *J. Geophys. Res.*, **106**, 14,701–14,710.
- Stewart, B. D., Pierazzo, E., Goldstein, D. B., Varghese, P. L. and Trafton, L. M. (2011). Simulations of a comet impact on the Moon and associated ice deposition in polar cold traps. *Icarus*, **215**, 1–16.
- Sun, X. and Neumann, G. A. (2015). Calibration of the Mercury Laser Altimeter on the MESSENGER spacecraft. *IEEE Trans. Geosci. Remote Sensing*, **53**, 2860–2874.
- Susorney, H. C. M., Barnouin, O. S., Ernst, C. M. and Johnson, C. L. (2016). Morphometry of impact craters on Mercury from MESSENGER altimetry and imaging. *Icarus*, **271**, 180–193.
- Susorney, H. C. M., James, P. B., Chabot, N. L., Ernst, C. M., Mazarico, E. M. and Neumann, G. A. (2017). Measuring the thickness of Mercury's polar water ice deposits using the Mercury Laser Altimeter. *Lunar Planet. Sci.*, **48**, abstract 2059.
- Talpe, M. J., Zuber, M. T., Yang, D., Neumann, G. A., Solomon, S. C., Mazarico, E. and Vilas, F. (2012). Characterization of the morphometry of impact craters hosting polar deposits in Mercury's north polar region. *J. Geophys. Res.*, **117**, E00L13, doi:10.1029/2012je004155.
- Teodoro, L. F. A., Eke, V. R. and Elphic R. C. (2010). Spatial distribution of lunar polar hydrogen deposits after KAGUYA (SELENE). *Geophys. Res. Lett.*, **37**, L12201, doi:10.1029/2010GL042889.
- Thomas, G. E. (1974). Mercury: Does its atmosphere contain water? *Science*, **183**, 1197–1198.
- Thomson, B. J., Bussey, D. B. J., Neish, C. D., Cahill, J. T. S., Heggy, E., Kirk, R. L., Patterson, G. W., Raney, R. K., Spudis, P. D., Thompson, T. W. and Ustinov, E. A. (2012). An upper limit for ice in Shackleton crater as revealed by LRO Mini-RF orbital radar. *Geophys. Res. Lett.*, **39**, L14201, doi:10.1029/2012GL052119.
- Urey, H. C. (1952). *The Planets: Their Origin and Development*. New Haven, CT: Yale University Press, 245 pp.
- Vasavada, A. R., Paige, D. A. and Wood, S. E. (1999). Near-surface temperatures on Mercury and the Moon and the stability of polar ice deposits. *Icarus*, **141**, 179–193.
- Vilas, F., Cobain, P. S., Barlow, N. G. and Lederer, S. M. (2005). How much material do the radar-bright craters at the Mercurian poles contain? *Planet. Space Sci.*, **53**, 1496–1500.
- Watson, K. B., Murray, C. and Brown, H. (1961). The behavior of volatiles on the lunar surface. *J. Geophys. Res.*, **66**, 3033–3045.
- Xiao, Z., Prieur, N. C. and Werner, S. C. (2016). The self-secondary crater population of the Hokusai crater on Mercury. *Geophys. Res. Lett.*, **43**, 7424–7432, doi:10.1002/2016GL069868.
- Yoldi, Z., Pommerol, A., Jost, B., Poch, O., Gouman, J. and Thomas, N. (2015). VIS-NIR reflectance of water ice/regolith analogue mixtures and implications for the detectability of ice mixed within planetary regoliths. *Geophys. Res. Lett.*, **42**, 6205–6212, doi:10.1002/2015GL064780.
- Zhang, J. A. and Paige, D. A. (2009). Cold-trapped organic compounds at the poles of the Moon and Mercury: Implications for origins. *Geophys. Res. Lett.*, **36**, L16203, doi:10.1029/2009GL038614.
- Zhang, J. A. and Paige, D. A. (2010). Correction to “Cold-trapped organic compounds at the poles of the Moon and Mercury: Implications for origins.” *Geophys. Res. Lett.*, **37**, L03203, doi:10.1029/2009GL041806.
- Zolotov, M. Yu. (2011). On the chemistry of mantle and magmatic volatiles on Mercury. *Icarus*, **212**, 24–41.